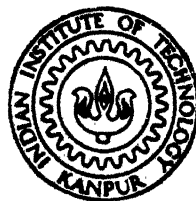


STEREOLOGY OF SINTERING OF METAL POWDERS

by
M. BASAVAIAH



DEPARTMENT OF METALLURGICAL ENGINEERING

INDIAN INSTITUTE OF TECHNOLOGY, KANPUR

JULY, 1987

ME

1987

M

BAS

STE

STEREOLOGY OF SINTERING OF METAL POWDERS

A Thesis Submitted
In Partial Fulfilment of the Requirements
for the Degree of

MASTER OF TECHNOLOGY

by
M. BASAVAIAH

to the

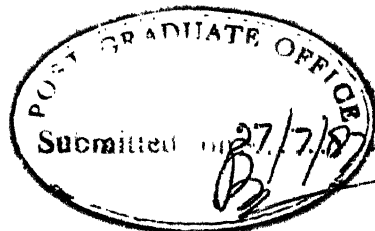
**DEPARTMENT OF METALLURGICAL ENGINEERING
INDIAN INSTITUTE OF TECHNOLOGY, KANPUR**

JULY, 1987

22 SEP 1987
CENTRAL LIBRARY
Acc. No. A 97985

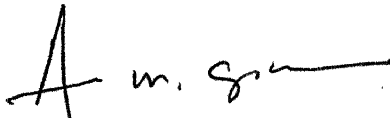
THU
GUY
1988

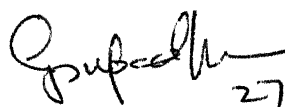
ME - 1987 - M - BAS - STE



CERTIFICATE

This is to certify that the present work entitled
"Stereology of Sintering of Metal Powders" has been carried
out by M. Basavaiah under our supervision and it has not been
submitted elsewhere for a degree.


A. M. GOKHALE
Assistant Professor
Dept. of Met. Engg.
Indian Institute of Technology
Kanpur 208016, INDIA


G. S. UPADHYAYA
Professor
Dept. of Met. Engg.
Indian Institute of Technology
Kanpur 208016, INDIA

ACKNOWLEDGEMENTS

I wish to express my deep sense of gratitude to Dr. G.S. Upadhyaya and Dr. A.M. Gokhale for their invaluable guidance and constant inspiration at every stages throughout the course of this work.

I sincerely acknowledge the help rendered to me by M/s S.C. Soni and K.P. Mukherjee.

I express thanks to all my friends for their co-operation and moral support during the course of this work.

I also thank M/s R.N. Srivastava and B.K. Jain for excellent typing and tracing work respectively.

- M. BASAVAI AH

CONTENTS

		Page
Chapter I	Literature Review	1
I.1	Introduction	1
I.2	Driving Force and Material Transport Mechanisms during Sintering	2
I.3	Model Experiments	4
I.4	Surface Diffusion Controlled Neck Growth	6
I.5	Scope of the Present Work	9
Chapter II	Experimental Procedures	10
II.1	Material	10
II.2	Sintering	10
II.3	Metallographic Preparation	11
II.3.1	Impregnation	11
II.3.2	Polishing	11
II.4	Stereology	11
II.4.1	The line intercept count	13
II.4.2	The triple point count	13
Chapter III	Experimental Results	14
III.1	Hydrogen Atmosphere Sintering	14
III.1.1	Volume fraction of porosity	14
III.1.2	Quantitative Metallographic Parameters	14
III.2	Argon Atmosphere Sintering	15
Chapter IV	Discussion	36
IV.1	Volume Fraction of Porosity	36

	Page
IV.2 Variation of Other Microstructural Parameters	36
Chapter V Conclusions	48
References	50
Appendix I	51

ABSTRACT

The various theories proposed earlier, to study kinetics of sintering, predict the time dependence of neck growth. Most of them are based on two particle systems, for example, neck growth during sintering of two spheres, or a sphere on a flat substrate etc. However, in the real systems, many particles are sintered together simultaneously. In the present study, the model proposed by Kuczynski for surface diffusion controlled neck growth has been studied experimentally to verify its applicability to sintering of narrow size range spherical iron powder via quantitative metallography.

Sintering was carried out at different temperatures in hydrogen as well as argon for different periods ranging from 0 to 34 h. The kinetics were monitored by measuring various stereological parameters like, total neck perimeter per unit volume (L_V), planar area enclosed by neck perimeter (A_V) and square of planar area enclosed by neck perimeter $[A^2]_V$ per unit volume. All these three independent parameters behaved with sintering period in accordance with Kuczynski model. Experimentally calculated values of kinetic constant were compared with theoretically predicted values, which showed reasonably good agreement. It has been concluded that the model proposed by Kuczynski for surface diffusion controlled neck growth is applicable to sintering of many particle system of close size range spherical iron powder.

Chapter I

LITERATURE REVIEW

I.1 INTRODUCTION

In the last half century, the Sintering Technology has been studied thoroughly down to fine details, but there are still some important gaps in the understanding of fundamental processes, and there still does not exist a definitive theory of the sintering process. The reason for the lack of an exact quantitative analysis is the complex interaction of geometrical and thermodynamic factors and the effect of a number of process variables which occur simultaneously or in the sequence. The main aim of any theoretical treatment of sintering process is to determine the mechanisms of material transport, to find out interrelation of various sintering parameters, such as sintering temperature, period and particle size.

Most of the earlier experiments to verify the theories of sintering were based on two particle systems, for example neck growth during sintering of two spheres or a sphere on a flat substrate etc. These models had so many simplifying assumptions in their derivations that great uncertainties exist as to the interpretation of the results. However, in the sintering of real powder mass many particles are present and a given particle has more than one interparticle contact. It is the purpose of this investigation to determine if the simplistic theories of sintering are quantitatively applicable to the sintering of real powder mass.

1.2 DRIVING FORCE AND MATERIAL TRANSPORT MECHANISMS DURING SINTERING

Sintering may be defined as the process of heating or annealing treatment by which powders are consolidated into coherent and/or dense polycrystalline aggregates.

The principal driving force for sintering is the lowering of free energy when particles grow together, voids shrink and the total surface energy of the aggregate decreases. The simplest experiments performed on the powder compacts, such as measurement of volume changes during sintering led to the conclusion that these changes must be a manifestation of some unbalanced forces acting between particles in the compacts interior and these forces are the same as those which cause spheroidisation of liquid droplets and climb of liquids in capillary tubes namely, surface or capillary forces which try to reduce the total surface, and consequently the energy of the system.

If the interface between two phases is curved, it is subjected to local pressure or stress (σ), which is given by well known Laplace equation,

$$\sigma = \gamma \left(\frac{1}{r_1} + \frac{1}{r_2} \right) \quad (1.1)$$

where r_1 and r_2 are two principal radii of surface, γ is the surface energy. Looking from the side of material, a concave curvature is negative ($r < 0$) and a convex surface such as that of a sphere is defined as positive ($r > 0$). Under a concave surface tensile stresses ($\sigma < 0$) and under a convex surface compressive stresses exist.

The local stress causes the change of chemical potential in the phases separated by curved interface, which is given, for a single phase system by

$$\Delta\mu = \gamma V \left(\frac{1}{r_1} + \frac{1}{r_2} \right) \quad (1.2)$$

where V is the molar volume of the substance, and its gradient actuates diffusion currents¹.

From the equation (1.2) one obtains with the relation,

$$\mu - \mu_0 = RT \ln \frac{P}{P_0} \simeq RT \frac{P - P_0}{P_0}$$

The kelvin equation for the difference in partial pressures over a flat surface P_0 and over a curved surface P ²:

$$P - P_0 = \frac{\gamma P_0 V}{RT} \cdot \left(\frac{1}{r_1} + \frac{1}{r_2} \right) \quad (1.3)$$

with the relation, $\mu - \mu_0 = -RT \ln \frac{C}{C_0} \simeq RT \cdot \frac{C_0 - C}{C_0}$, and from equation (1.2), we get the relation

$$C_0 - C = \frac{\gamma \cdot C_0 \cdot V}{RT} \left(\frac{1}{r_1} + \frac{1}{r_2} \right) \quad (1.4)$$

This equation describes the difference in vacancy concentration under a curved surface C and under a flat surface C_0 . It shows that under a concave surface vacancy concentration is higher than that under a flat surface but under a convex surface it is lower.

Identification of the flow of mechanism is done by mathematical analysis of flow leading to the equations linking some easily measurable variables, such as neck radius x , sintering period t and temperature T .

Solutions to the mathematical models yield well known fundamental equations¹ which link the increase of the radius x of a neck formed between two spheres of identical radius R , with the sintering period t ,

$$\left(\frac{x}{R}\right)^n = \frac{F(T)}{R^m} \cdot t \quad (1.5)$$

where $F(T)$ is appropriate function of temperature which contains the proper coefficient characterising given flow and exponents 'm' and 'n' characterize predominant flow responsible for welding of two particles together. The values of m and n corresponding to various mechanism are listed in Table 1.1. The relationships given by equation (1.5) were verified^{by} model experiments^{1,3,4} on the systems composed of combinations of spherical particles, spherical particle-plates and wire and wires-cylinders. The essential feature of this method is direct measurement of neck radius x in the metallographic section. By such experiments it has been established that the predominant mechanism of sintering of metallic particles is volume diffusion.^{1,4,6} Fine metallic particles or wires sinter by surface diffusion.^{1,5,12}

I.3 MODEL EXPERIMENTS

The models given by equation (1.5) are based on two particle systems and the model experiments carried out to verify the above models were based on sintering of two spheres, sphere to plate or wires and wire-plates.^{1,4,5,6,12}

Johnson^{7,8} indicated how the sintering of two spheres could be described quantitatively under conditions of simultaneous transport by surface, grain boundary and volume diffusion.

Table 1.1

Exponents m and n and corresponding sintering mechanisms¹⁴

m	n	Mechanism
1	2	Newtonian flow
2	3	Transport through the external phase
3	5	Diffusion through crystals volume
4	6	Grain boundary diffusion
4	7	Surface diffusion

In these models of two particle systems, the description of neck geometry is done by a simple tangent circle approximation.

A similar model has been postulated by Ashby⁹ for simultaneous flows to determine the effectiveness of various transport mechanisms in the so-called sintering diagrams, boundaries along which two mechanisms contribute equally strongly to material transport, are shown as a function of sintering time, temperature, neck radius and particle size.

On the basis of existing sintering theories discussed in earlier sections, Ashby assumes that the total neck growth rate in the initial sintering stage \dot{x}_t is the sum of all the neck growth rates obtained by elementary processes, i.e.,

$$\dot{x}_t = \sum_{i=1}^n \dot{x}_t$$

Then the sintering conditions (temperature-time-neck size) are calculated at which one process contributes exactly 50% to neck

growth. Ashby's concept is very useful in the estimation of the role of individual mechanisms as well as in the prognosis of the material behaviour during sintering and hot pressing. The main drawback is the difficulty of establishing the necessary physical constants in the rate equations, because even slight variation of this constants may considerably change the character of sintering diagrams.

The other problem which is widely neglected is the fact that the rate equations are derived entirely on basis of the two sphere models and the tangent circle approximation and therefore care should be taken when applying them to real powders.

1.4 SURFACE DIFFUSION CONTROLLED NECK GROWTH

Surface diffusion leads to neck formation without shrinkage. This is schematically shown in Figure 1.1. The classical relation between neck radius x , and sintering time t given by Kuczynski¹ can be derived as follows¹³:

With a given gradient of the chemical potential the flux is determined by the coefficient of the surface self diffusion D_s in a certain sub-surface layer δ_s . The rate of volume change in the contact area is given by,

$$\frac{dV}{dt} = J_s S \quad (1.6)$$

where J_s is the flux of the surface self-diffusion

$S = 2\pi x \delta_s$ the surface through which the flux is materialized

and also we have $dV = S_0 dx$

where S_0 is the neck surface, V and S_0 of neck are given

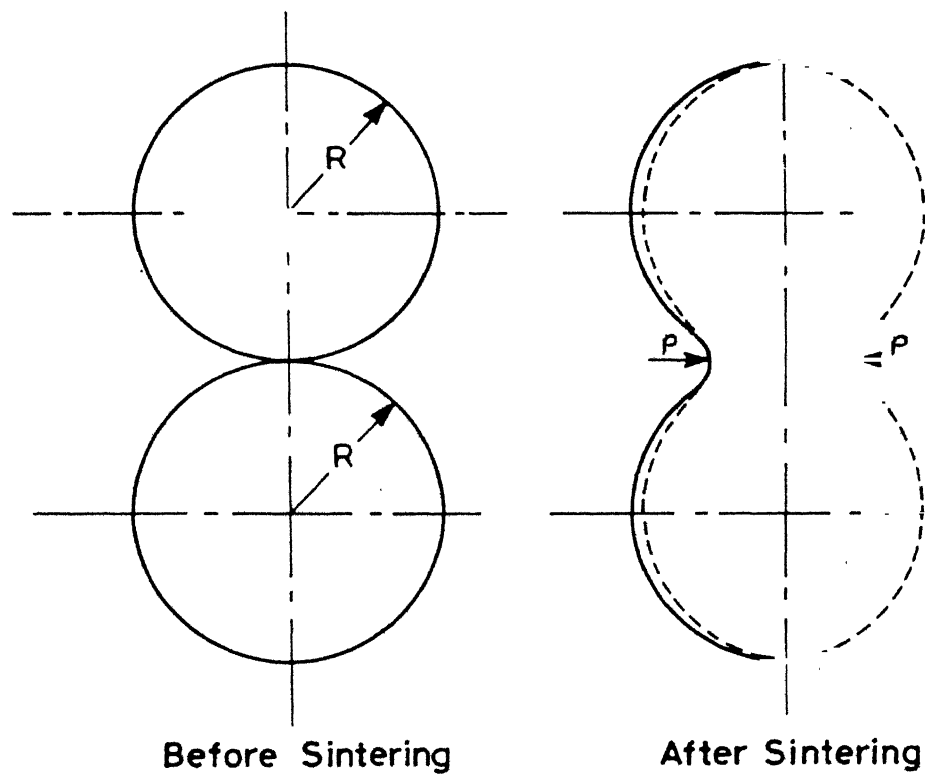


Fig 1.1 SURFACE DIFFUSION CONTROLLED SINTERING

respectively by $\frac{\pi x^4}{2R}$ and $\frac{2\pi x^3}{R}$.

It follows from equation (1.6) that,

$$\frac{dx}{dt} = J_s \cdot \frac{S}{S_0} = J_s \frac{2\pi x \delta_s}{2\pi x^3/R} = J_s \frac{\delta_s R}{x^2} \quad (1.7)$$

with

$$J_s = -D_s \frac{\nabla \mu}{kT} = -D_s \frac{2\gamma \delta_s^3}{kT} \nabla \left(-\frac{1}{\rho}\right) \quad (1.8)$$

where δ = interatomic distance, we get

$$\frac{dx}{dt} = -D_s \frac{2\gamma \delta_s^3}{kT} \frac{\delta_s R}{x^2} \frac{1}{\rho^2} \quad (1.9)$$

Taking into account the relation between ρ and x i.e. $\rho = \frac{x^2}{2R}$ and by integrating we get the following relation^{1,13}

$$x^7 = \frac{56 R^3 \gamma D_s \delta_s^4}{kT} \cdot t \quad (1.10)$$

This equation predicts that in the case of surface diffusion controlled neck growth, neck radius grows with seventh root of sintering time t .

In the literature we find different equation of sintering kinetics for surface diffusion viz.

$$x^7 \propto t \quad \text{Knczynski}^1$$

$$x^5 \propto t \quad \text{Cabrera}^{10}$$

$$x^3 \text{ and } x^5 \propto t \quad \text{Schwed}^{11}$$

$$x^6 \propto t \quad \text{Pines}^{12}$$

It has been explained by Rockland¹² that this disagreement is due to the fact that the different researchers used various

simplifications, for example, in defining the geometry of the system, and confirms that Kuczynski's solution is correct.

All these simple relationships hold if the neck geometry is approximated by a circle tangent to the original surface. This approximation has the drawback that the volume of the system is not constant during sintering but grows by the neck volume.

I.5 SCOPE OF THE PRESENT WORK

Although much work has been done on model experiments to understand the material transport mechanisms during sintering, there are only a few attempts made in the last three decades to apply simplistic models of two particle systems to the real systems.

In the present work, an attempt has been made to study critically the kinetics of surface diffusion controlled neck growth during initial stages of sintering of loose packed spherical iron powder. Various metallographic measurements like ^{neck perimeter} per unit volume, surface area per unit volume etc. have been done to correlate with the Kuczynski's model.

Chapter II

EXPERIMENTAL PROCEDURES

II.1 MATERIAL

Spherical iron powder (grade C1018), used in the present investigation, was supplied by Nuclear Metals Inc. of U.S.A. which was prepared by Rotating Electrode Process. The particle size of the supplied powder was $-210\text{ }\mu\text{m}$ (-70 mesh). This powder was sieved to get close size range of $74\text{ }\mu\text{m} - 62\text{ }\mu\text{m}$ ($-200 + 250$ mesh). Size analysis of this close size range powder was done on Coulter Counter (Model Z_B and B).

II.2 SINTERING

The powder was filled in graphite mould of dimensions: 14 mm height; 8.2 mm interval diameter, which was kept in an inconel boat. The powder filled mould was put into inconel boat filled with coarse refractory grade alumina powder to provide stability to the former, while pushing the boat into the furnace tube. The sintering was carried out in a laboratory type silicon carbide heated tubular furnace at temperatures of 950°C , 1000°C , 1050°C respectively with a control of $\pm 5^\circ\text{C}$ for different periods under isothermal condition ranging from 0 to 34 h. Dry hydrogen and argon were used as sintering atmospheres. The dew points of hydrogen and argon were measured on Shaw Automatic Dew Point (SADP) meter, which gave values of -26°C , -32°C respectively.

After sintering, the cylindrical compacts were ejected out of the graphite mould and densities were calculated after measuring the mass and physical dimensions.

II.3 METALLOGRAPHIC PREPARATION

II.3.1 IMPREGNATION

To avoid smearing of pores and for sufficient strength during metallographic preparation the sintered samples were impregnated with an epoxy resin as follows: The epoxy resin of grade CY 212 Araldite, was mixed thoroughly with 10% hardner in a plastic container. Then the sintered samples were immersed in the mixture and were kept under vacuum (10^{-2} torr) for about 20 minutes to ensure complete impregnation. Then the sample were taken out and were given enough time to get hardened.

II.3.2 POLISHING

The hardened samples were ground on belt grinder to get longitudinal section. Those were then wet polished on the LUNN MAJOR unit over 220, 320, 500 and 1000 grit number silicon carbide papers followed by fine wheel polishing with suspended 0.3 μ m size alumina powder in distilled water.

II.4 STEREOLOGY

Stereological measurements like area fraction of pores, the line intercept count N_L , the triple point count P_A , length of chords through necks were made on Bauch and Lomb ALPHA 500 type image analyser, at a magnification of 700X.

When the sample is cut, due to spherical shape of powder, the necks are clearly seen in the plane of polish. Figure 2.1 shows the stereological parameters measured in the present investigation.

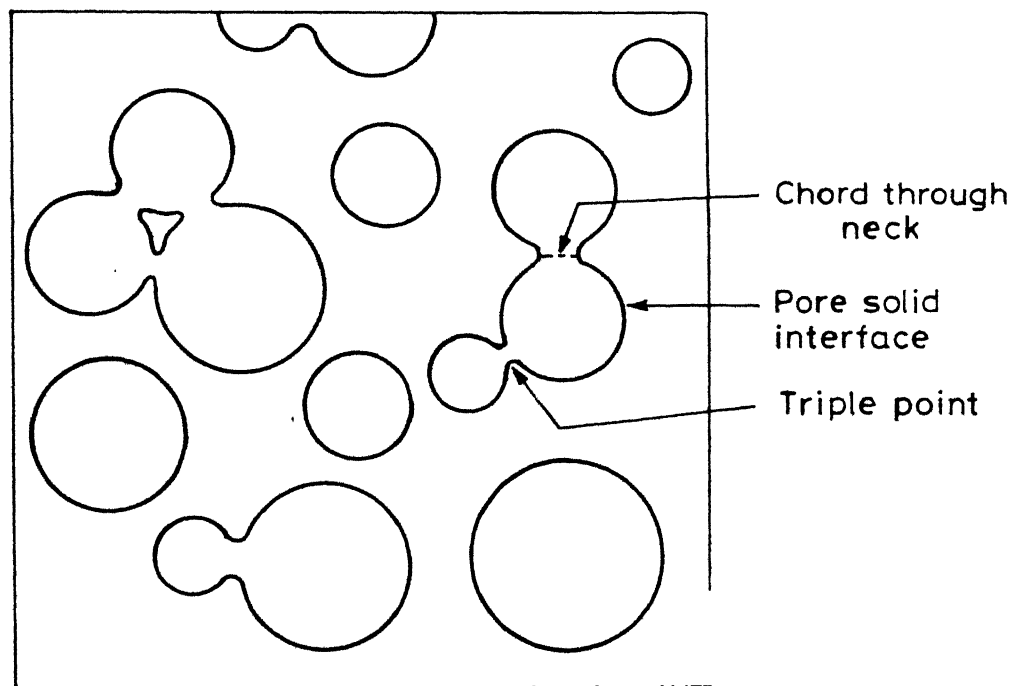


Figure 2.1 A schematic microstructure in the plane of polish.

II.4.1 THE LINE INTERCEPT COUNT N_L

A grid of concentric circles was superimposed on the TV screen. These test lines were scanned, and the number of times they cross the traces of pore-solid interface or particle-particle interface as the case may be was counted. The real length (actual length as superimposed on the structure) of these test lines was calculated using a calibration grid. The average value of N_L was obtained by summing the counts on individual areas, and dividing by the total length of test lines of grid for all the observations.

II.4.2 THE TRIPLE POINT COUNT P_A

The solid-solid-pore triple line circles appear as the points on metallographic sectioning plane. The number of triple points was counted on each observation. The average value of P_A was obtained by summing the counts for each observation, and dividing by the total actual area scanned.

The shortest distances between two triple points in the plane polish give the chord lengths through solid-solid-pore triple line circles. Chord lengths need not be equal to the diameter of the circle. These lengths were measured manually on the TV screen of the image analyser. Measurements were made in 100 frames, each with an area of 0.0028 cm^2 .

Chapter III

EXPERIMENTAL RESULTS

III.1 HYDROGEN ATMOSPHERE SINTERING

The optical micrographs of the compacts after sintering at 1050°C in hydrogen for different periods are shown in Figure 3.1.

From the various measurements discussed in the previous chapter the following geometric parameters were calculated as follows.

III.1.1 Volume fraction of porosity (V_V)

It is directly given by area fraction (A_A) measurements according to the relation of stereology,

$$V_V = A_A$$

It was also calculated from the sintered density obtained after measuring the mass and dimensions of sintered specimens, which are correlated as,

$$\text{Volume fraction of porosity} = 1 - \frac{\text{Sintered density}}{\text{Theoretical density of the material}}$$

These two values are given in Table 3.1 for comparison. The plots of volume fraction porosity obtained by the above two methods are shown in Figure 3.2.

III.1.2 Quantitative Metallographic Parameters

All the parameters related to quantitative metallography are summarised in Tables 3.2 to 3.4.

Total neck perimeter (solid-solid-pore triple line) length per unit volume (L_V) was calculated from the triple point count (P_A) by the relation^{15,16}

$$L_V = 2P_A$$

In Figures 3.3 to 3.5 L_V is plotted against seventh root of sintering period $t^{1/7}$.

From the chord length measurements, the following parameters were calculated.

(a) Planar area enclosed by neck perimeter per unit volume (A_V): This was calculated from the average total chord length per section plane area (L_A) by using the relation^{15,16},

$$A_V = \frac{4}{\pi} L_A$$

Plots of A_V versus $t^{2/7}$ are shown in Figures 3.7 to 3.9.

(b) The square of the planar area enclosed by neck perimeter per unit volume $[A^2]_V$: This was determined by the relation¹⁷

$$[A^2]_V = \frac{1}{3} \cdot L_V \cdot \overline{l^3}$$

where $\overline{l^3}$ is the average of cubes of chord lengths.

This is plotted against $t^{4/7}$ and is shown in Figures 3.11 to 3.13.

III.2 ARGON ATMOSPHERE SINTERING

This was carried out at a temperature 1000°C, for different sintering period (under isothermal conditions) ranging from 0 to 24 h.

All the stereological parameter measurements related to sintered compacts were repeated like those sintered in hydrogen. The results are given in Table 3.5, while various plots are shown in Figures 3.6, 3.10 and 3.14.

Table 3.1

Volume Fraction of Porosity

Sintering Period (hrs)	Sintering temperature, atmosphere							
	950°C, H ₂		1000°C, H ₂		1050°C, H ₂		1000°C, Ar	
	Physical method	Metallo- graphic method	Physical method	Metallo- graphic method	Physical method	Metallo- graphic method	Physical method	Metallo- graphic method
0	0.42	0.41	0.38	0.42	0.40	0.35	0.39	0.37
0.17	0.39	0.39	0.40	0.45	0.40	0.37	0.41	0.38
0.50	-	-	0.41	0.46	-	-	-	-
0.75	-	-	0.43	0.46	-	-	-	-
1	0.41	0.39	-	-	0.38	0.37	0.40	0.37
4	0.40	0.37	-	-	0.41	0.36	0.40	0.37
8	-	-	0.41	0.50	-	-	-	-
16	0.40	0.37	0.41	0.50	0.40	0.39	0.40	0.38
24	0.40	0.40	0.43	0.48	0.39	0.36	0.40	0.35
34	-	-	0.40	0.40	-	-	-	-

Table 3.2

Stereological Parameters of Sintered Iron Powder in Hydrogen
(Sintering temperature 950°C)

Sintering period (hrs)	P_A $\times 10^{-3}$, cm^{-2}	L_A , cm/cm^2	$\overline{l^3}$ $\times 10^{10}$, cm^3	L_V $\times 10^{-3}$, cm/cm^3	A_V , cm^2/cm^3	$[A^2]_V$ $\times 10^6$, cm^4/cm^3
0.00	7.21	1.52	1.05	14.42	1.94	0.50
0.67	11.91	3.09	2.35	23.82	3.94	1.87
1.00	12.90	3.94	3.31	25.80	5.02	2.85
4.00	14.32	4.86	4.61	28.64	6.19	4.40
16.00	14.88	5.25	5.53	29.75	6.68	5.48
24.00	14.98	5.71	6.50	29.96	7.27	6.49

Table 3.3

Stereological Parameters of Sintered Iron Powder in Hydrogen
(Sintering temperature 1000°C)

Sintering period (hrs)	P_A $\times 10^{-3}$, cm^{-2}	L_A , cm/cm^2	\overline{V}^3 , $\times 10^{10}$, cm^3	L_V , $\times 10^{-3}$, cm/cm^3	A_V cm^2/cm^3	$[A^2]_V$ $\times 10^6$ cm^4/cm^3
0.00	4.94	1.23	2.48	9.88	1.57	0.82
0.67	10.30	3.15	3.19	20.60	4.01	2.19
0.50	11.18	3.47	3.41	22.36	4.42	2.54
0.75	11.26	3.35	3.04	22.52	4.27	2.29
8.00	13.98	6.31	9.73	27.96	8.03	9.07
16.00	14.98	6.61	9.36	29.96	8.42	9.35
24.00	18.14	8.96	13.12	36.28	11.41	15.86
34.00	16.96	7.42	9.80	33.92	9.45	11.08

Table 3.4

Stereological Parameters of Sintered Iron Powder in Hydrogen
(Sintering temperature 1050°C)

Sintering period (hrs)	$P_A,$ $\times 10^{-3},$ cm^{-2}	$L_A,$ cm/cm^2	$\overline{l^3},$ $\times 10^{10},$ cm^3	$L_V,$ $\times 10^{-3},$ cm/cm^3	$A_V,$ cm^2/cm^3	$[A^2]_V$ $\times 10^6,$ cm^4/cm^3
0.00	13.71	4.09	3.39	27.43	5.20	3.10
0.67	14.95	3.99	2.42	29.90	5.08	2.41
1.00	15.83	4.93	3.76	31.67	6.28	3.96
4.00	19.78	8.49	8.59	39.55	10.81	11.32
16.00	23.60	12.35	15.74	47.21	15.73	24.77
24.00	27.89	15.92	20.85	55.80	20.27	38.78

Table 3.5

Stereological Parameters of Sintered Iron Powder in Argon
(Sintering temperature 1000°C)

Sintering period, (hrs)	$P_A,$ $\times 10^{-3},$ cm^{-2}	$L_A,$ cm/cm^2	$\overline{V}_V^3,$ $\times 10^{10},$ cm^3	$L_V,$ $\times 10^{-3},$ cm/cm^3	$A_V,$ cm^2/cm^3	$[A^2]_V$ $\times 10^6,$ cm^4/cm^3
0.00	5.71	1.27	1.87	11.42	1.62	0.72
0.67	6.65	1.56	3.43	13.30	1.99	1.52
1.00	14.36	4.96	5.11	28.72	6.31	4.90
4.00	16.95	6.13	5.85	33.90	7.81	6.61
16.00	20.37	8.54	8.28	40.73	10.88	11.24
24.00	19.13	8.99	13.55	38.26	11.46	17.28

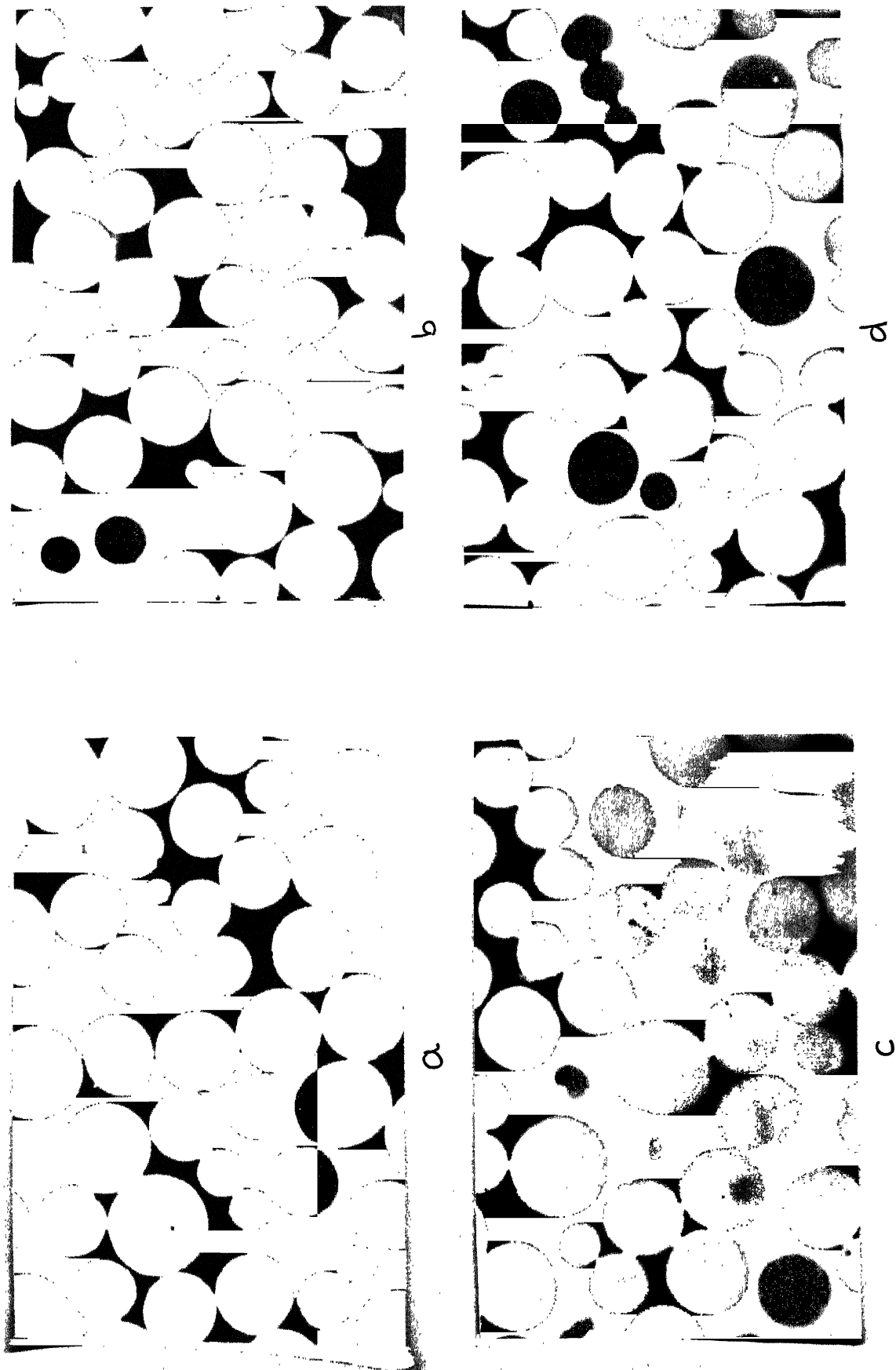


Figure 3.1 Evolution of microstructure during sintering of loose stacked spherical iron powder in hydrogen at 1050°C (a) sintered for 0 h, (b) sintered for 1 h, (c) sintered for 16 h, (d) sintered for 16 h

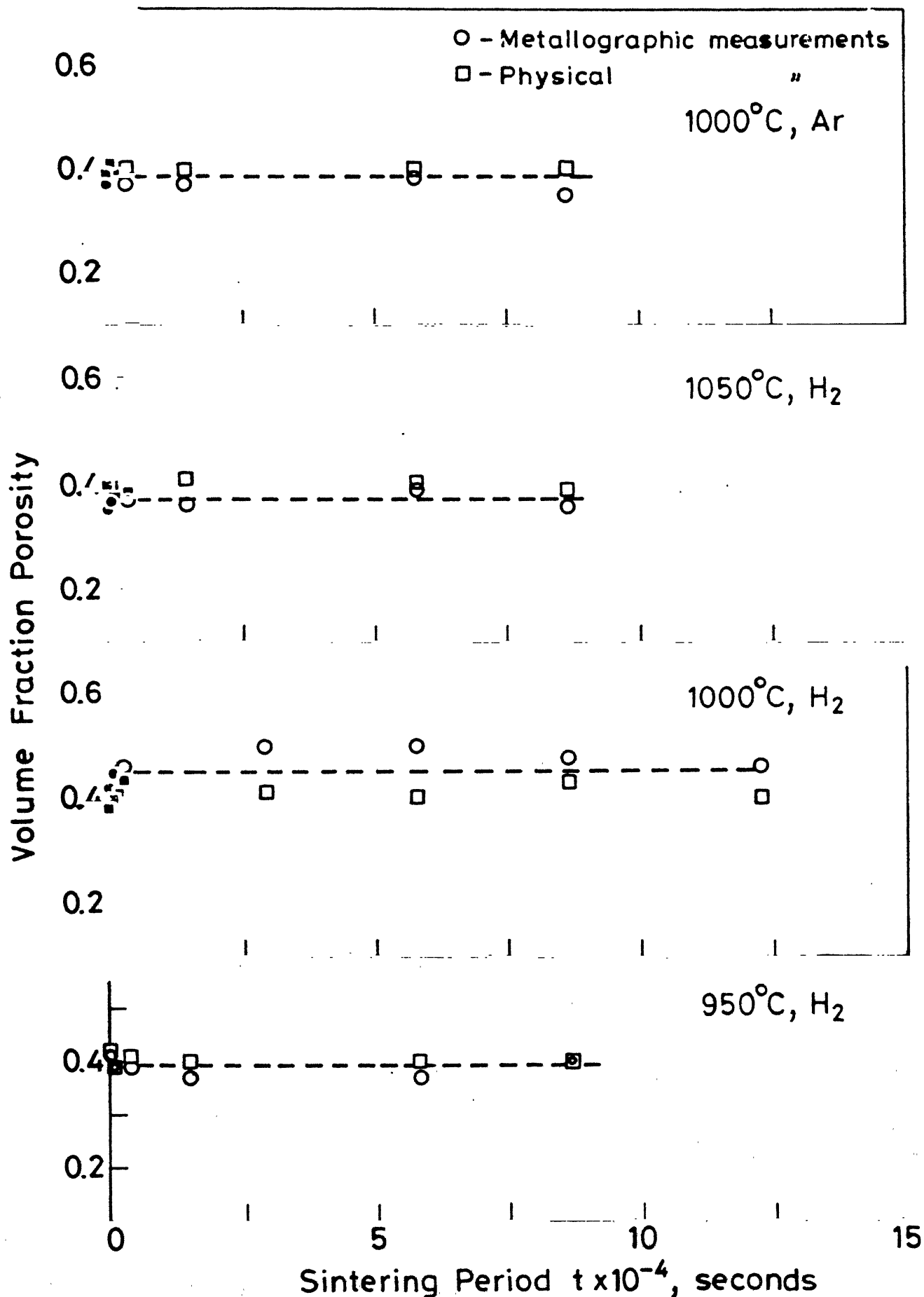


Figure 3.2 Variation of volume fraction porosity with sintering period of loose stacked spherical iron powder.

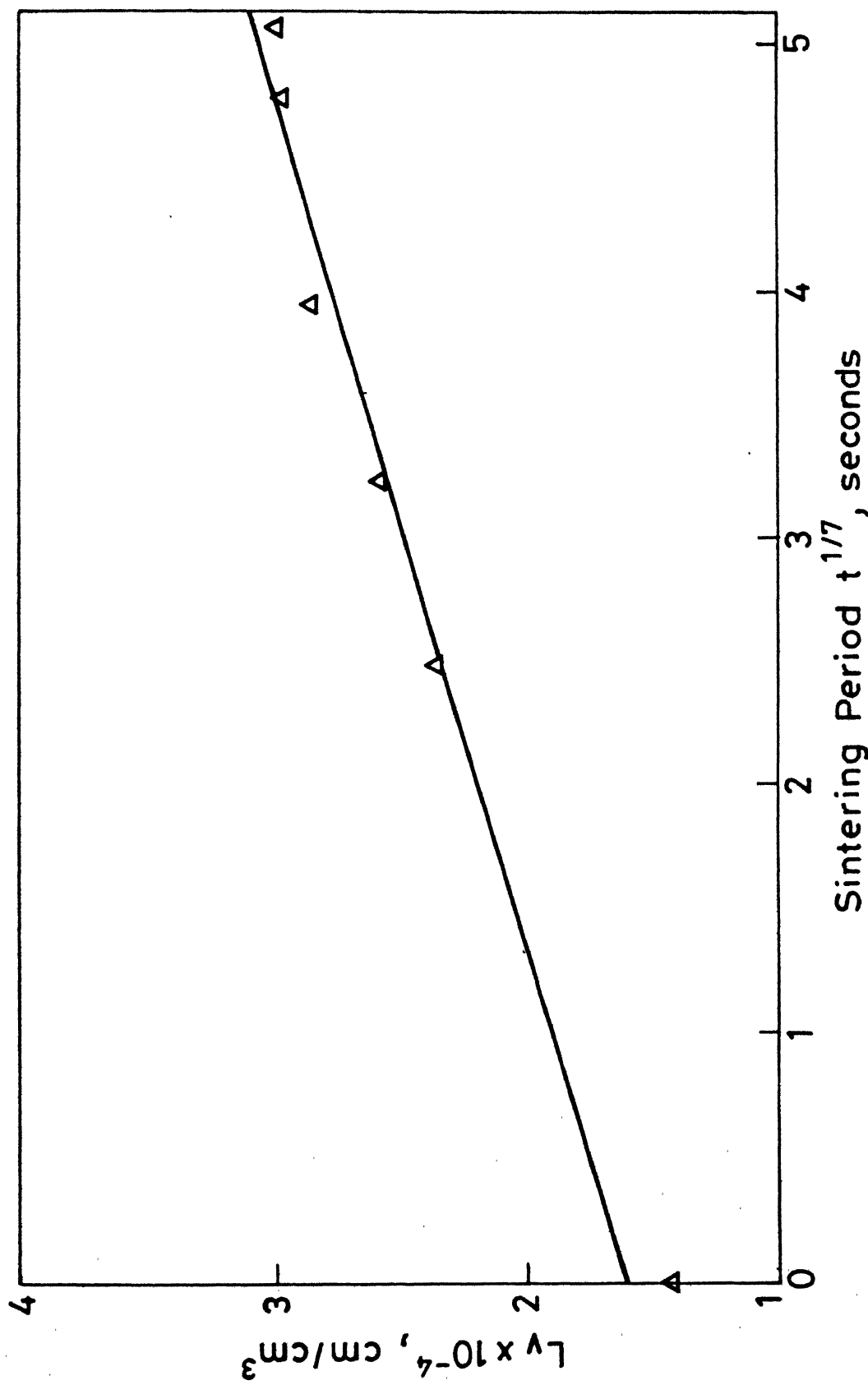


Figure 3.3 A plot of L_v vs. $t^{1/7}$ during sintering of loose stacked spherical iron powder in hydrogen at 950°C.

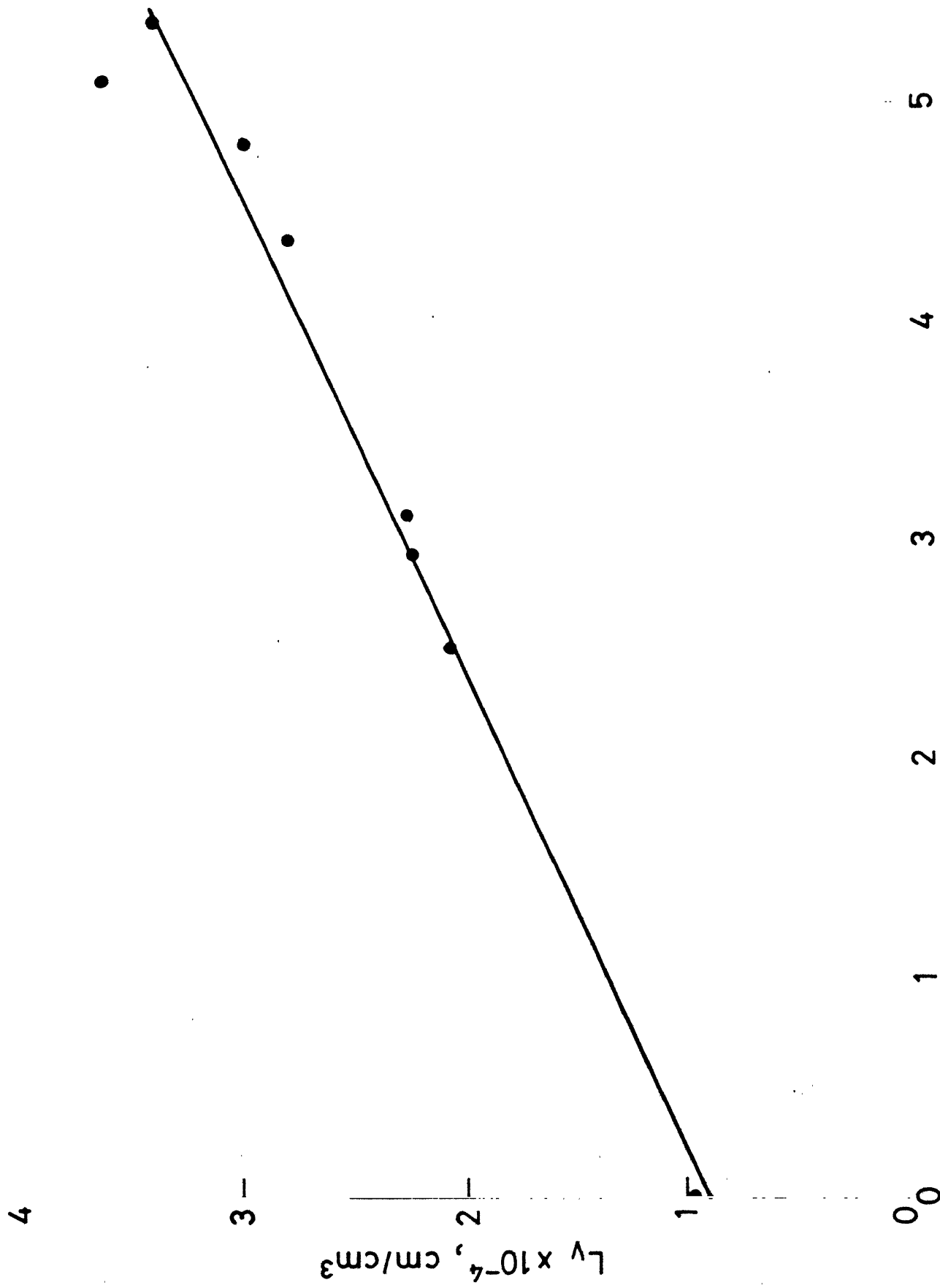


Figure 3.4 A plot of L_v vs. $t^{1/7}$ during sintering of loose stacked spherical iron powder in

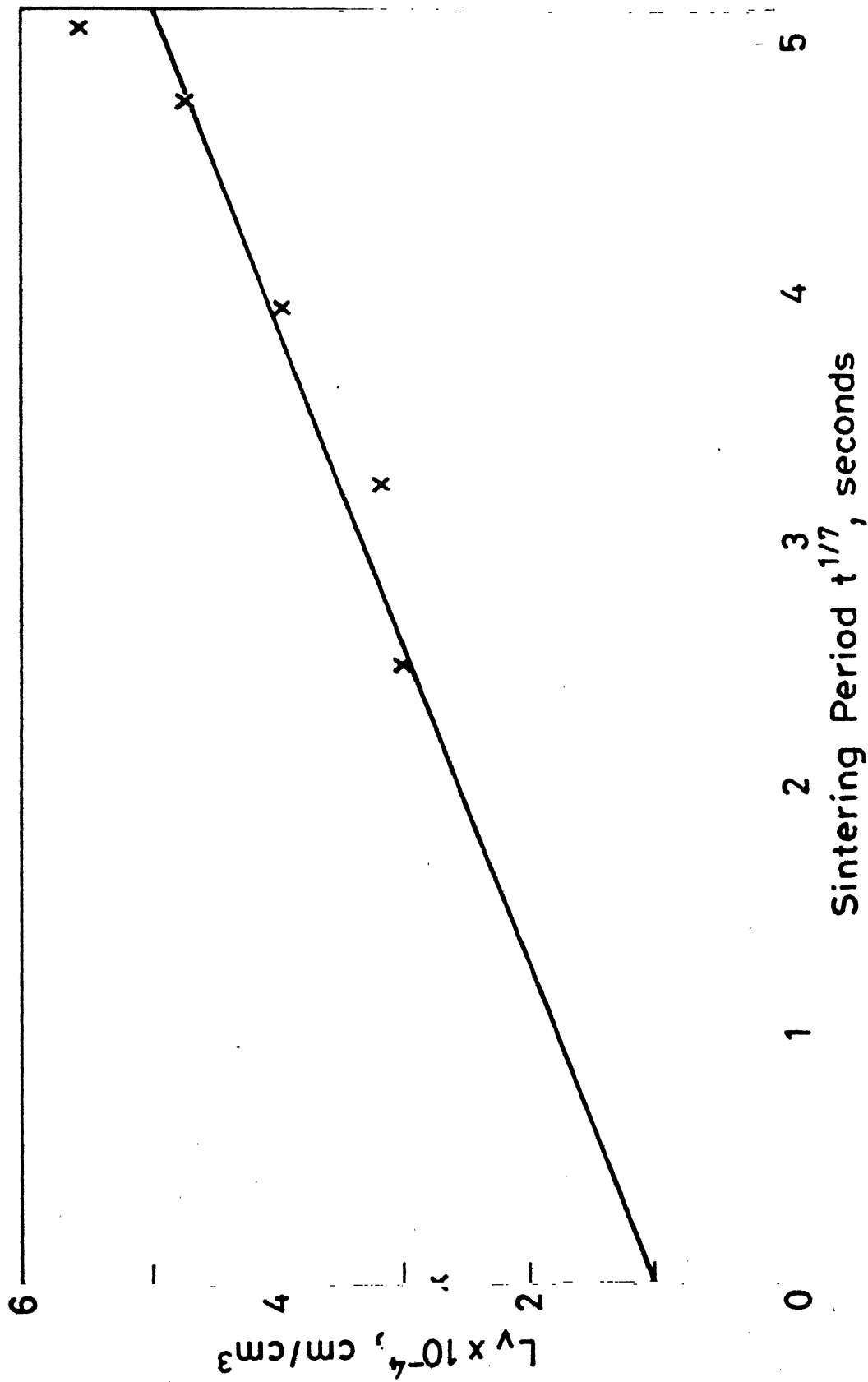


Figure 3.5 A plot of L_V vs. $t^{1/7}$ during sintering of loose stacked spherical iron powder in hydrogen at 1050°C .

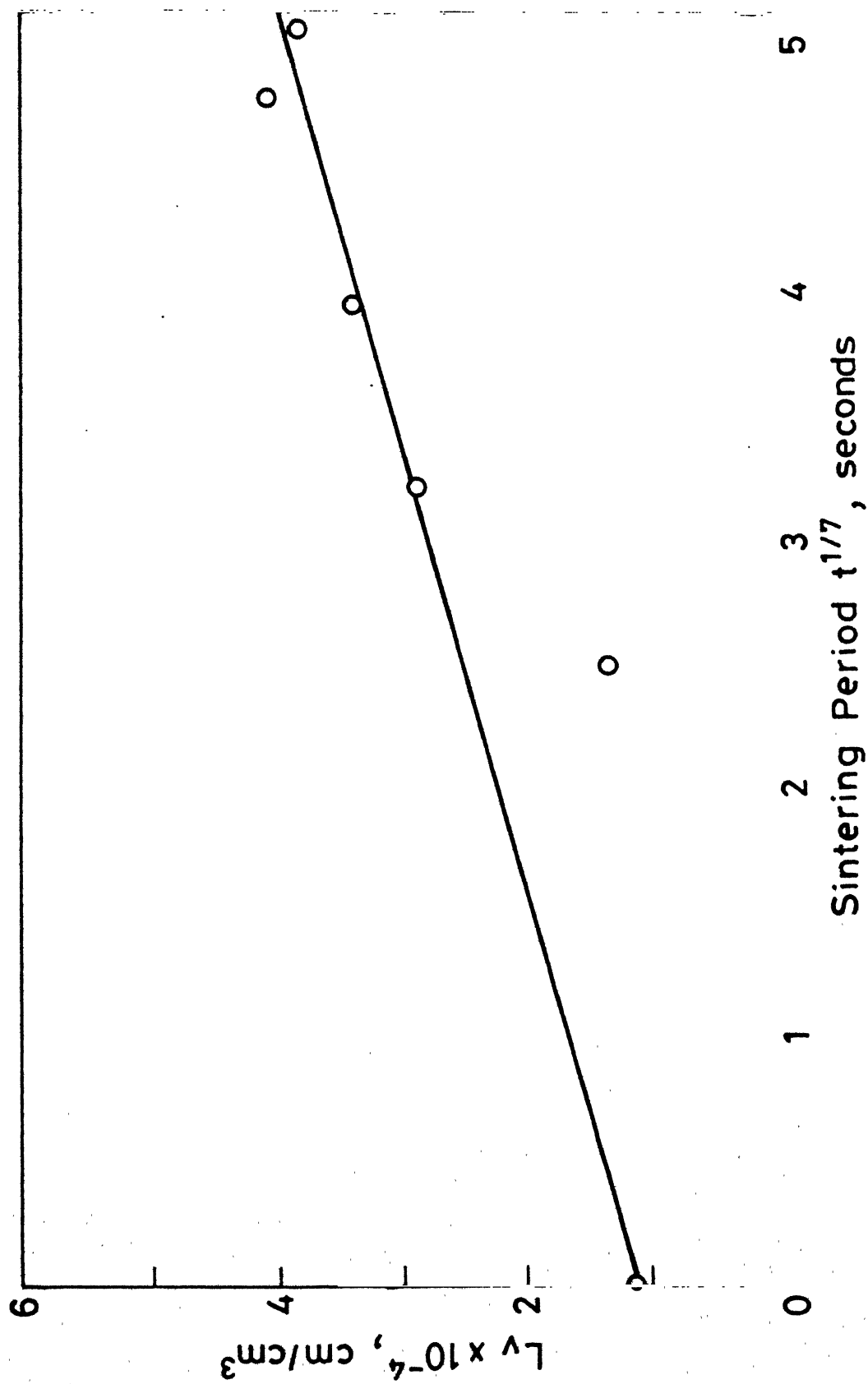


Figure 3.6 A plot of L_v vs. $t^{1/7}$ during sintering of loose stacked spherical iron powder in argon at 1000°C.

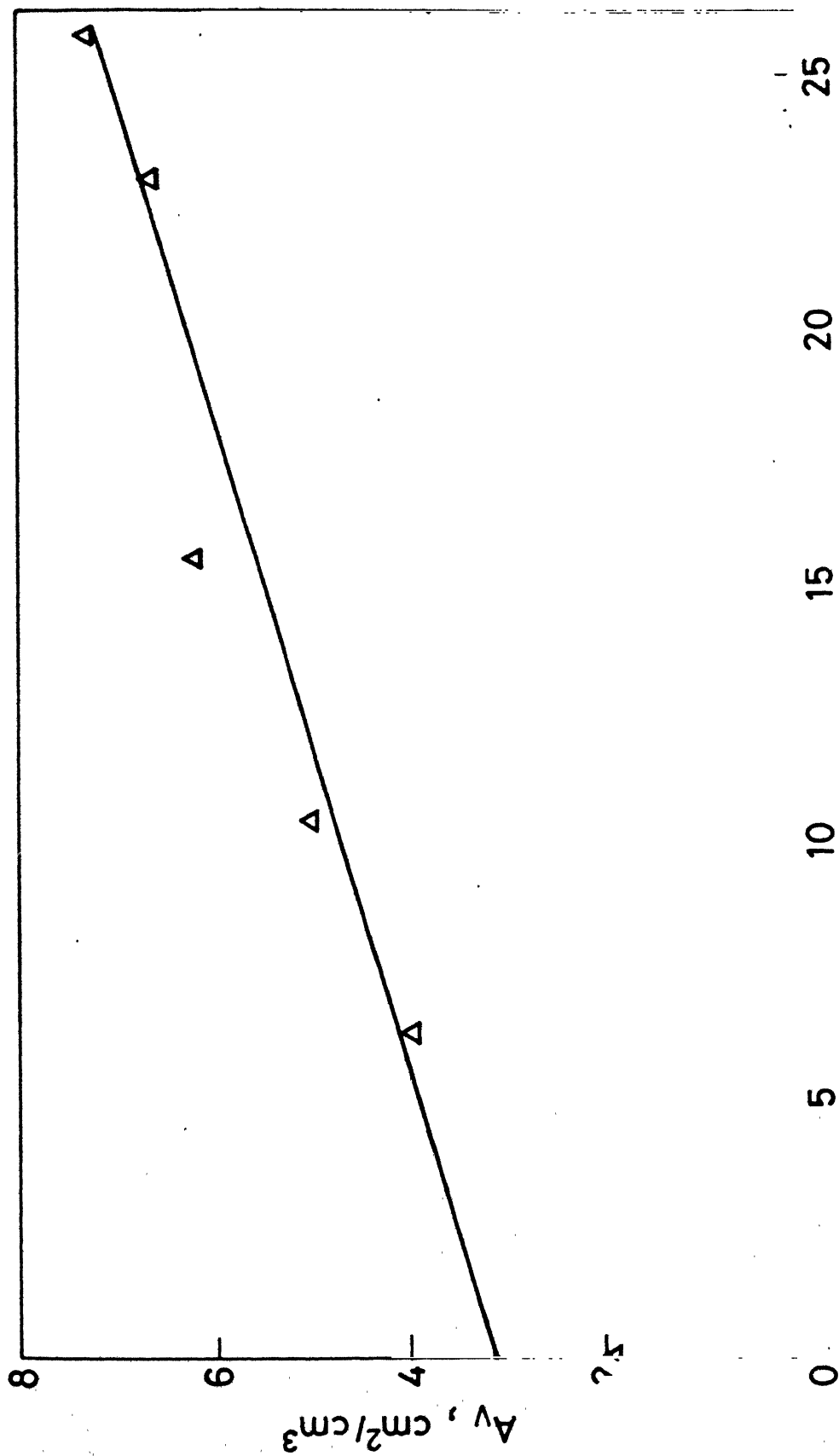


Figure 3.7 A plot of A_v vs. $t^{2/7}$ during sintering of loose stacked spherical iron powder in hydrogen at 950°C.

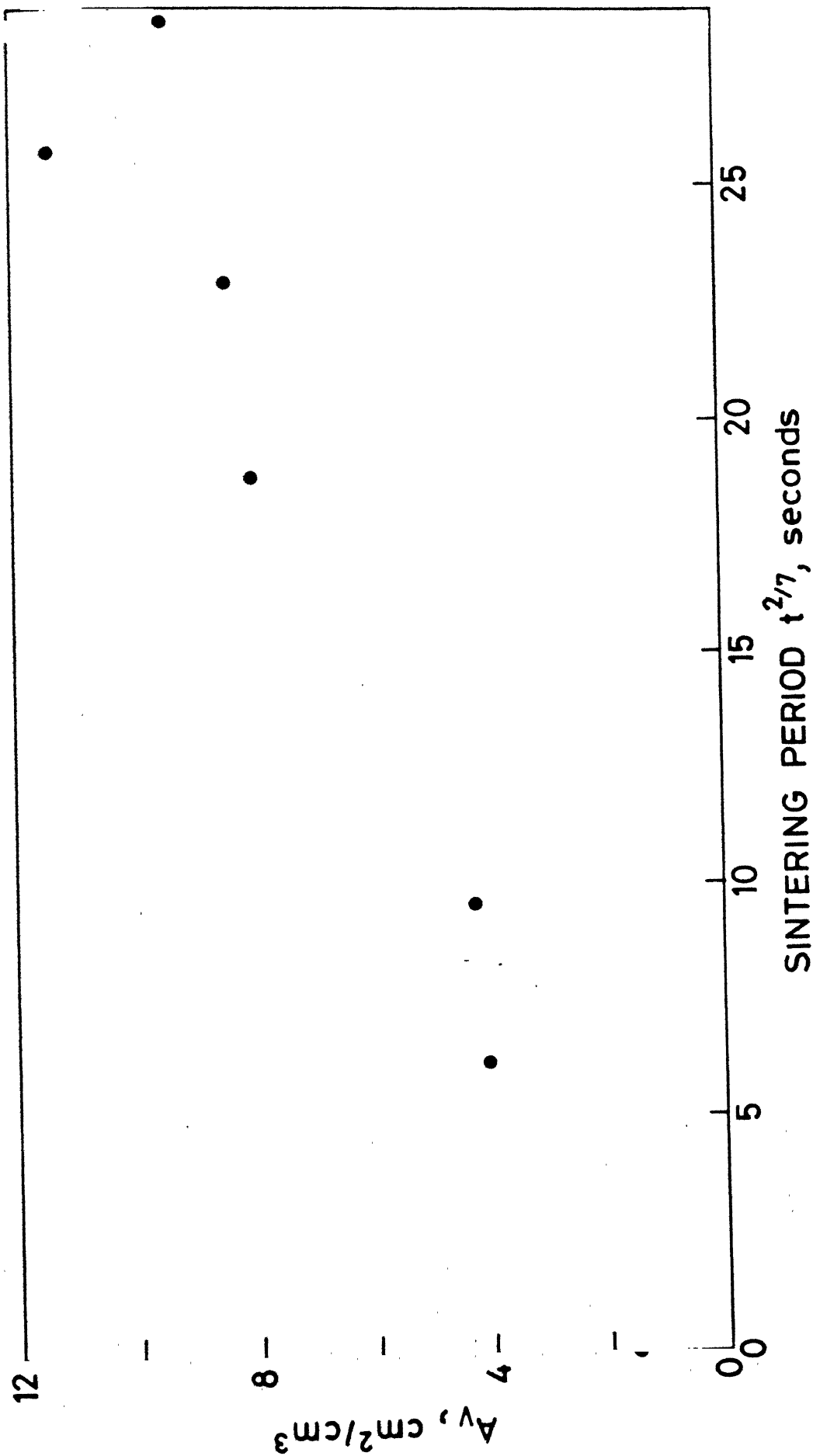


Figure 3.8 A plot of A_v vs. $t^{2/7}$ during sintering of loose stacked spherical powder in hydrogen at 1000°C.

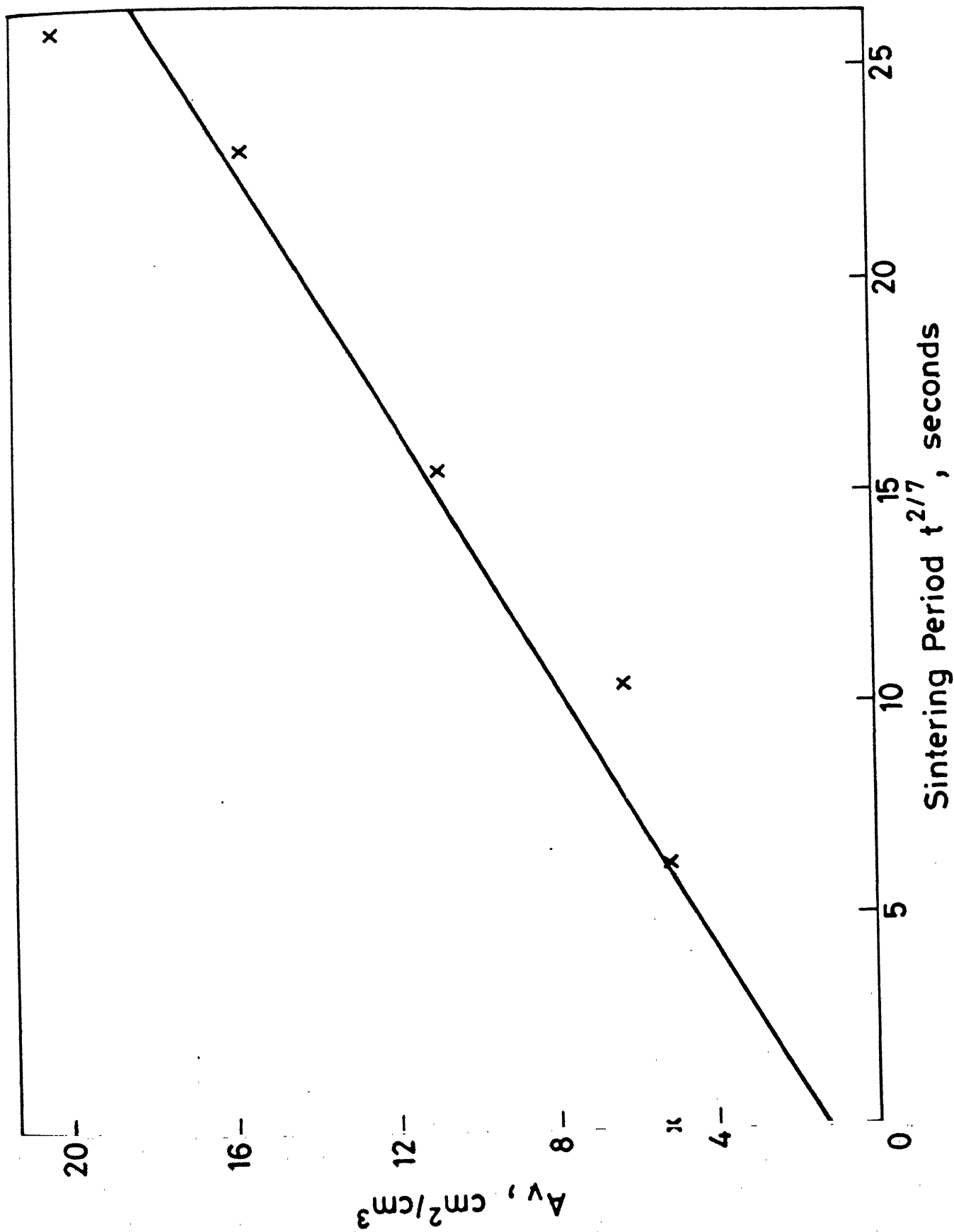


Figure 3.9 A plot of A_v vs. $t^{2/7}$ during sintering of loose stacked spherical iron powder

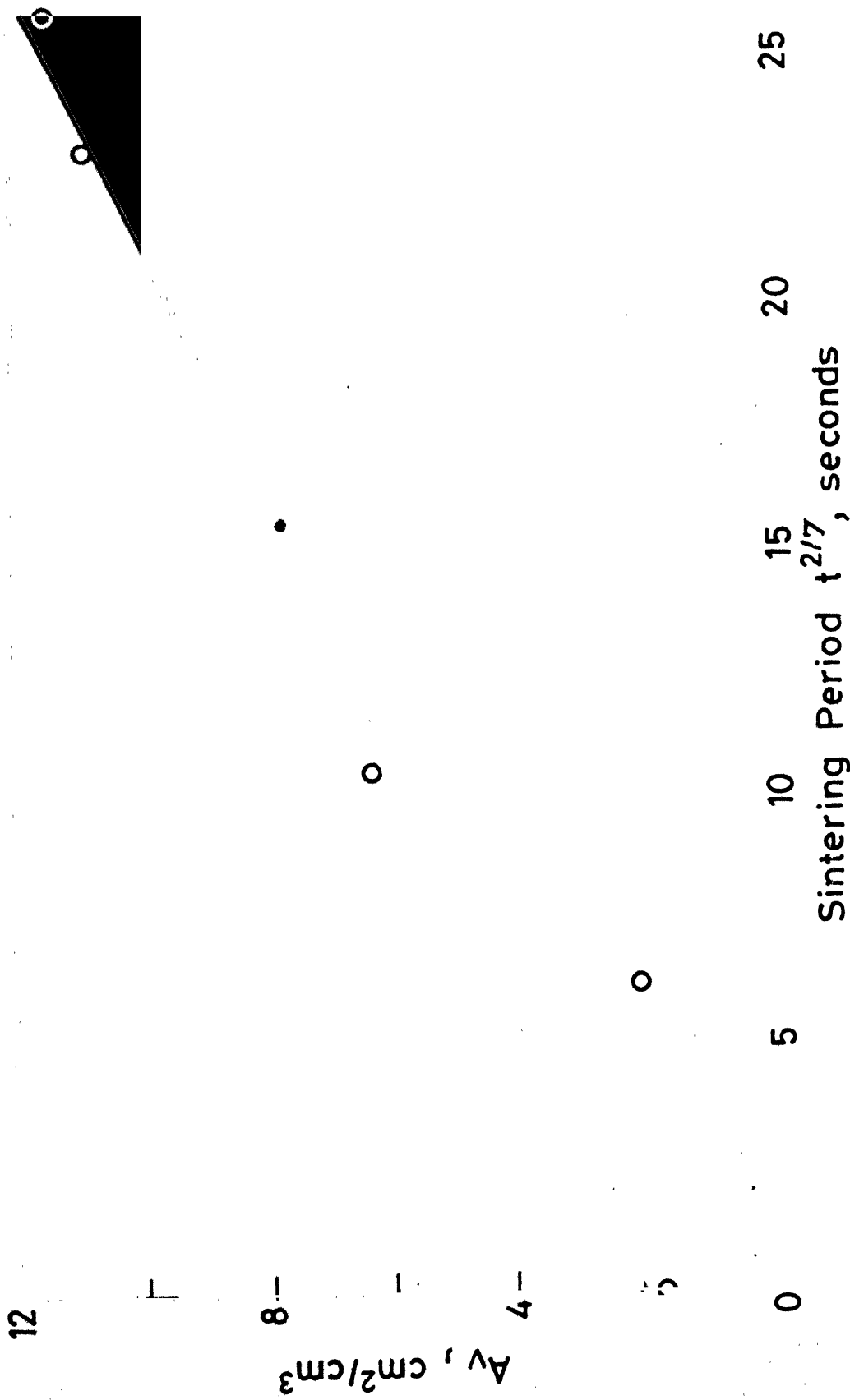


Figure 3.10 A plot of A_v vs. $t^{2/7}$ during sintering of loose stacked spherical iron powder in argon at 1000°C.

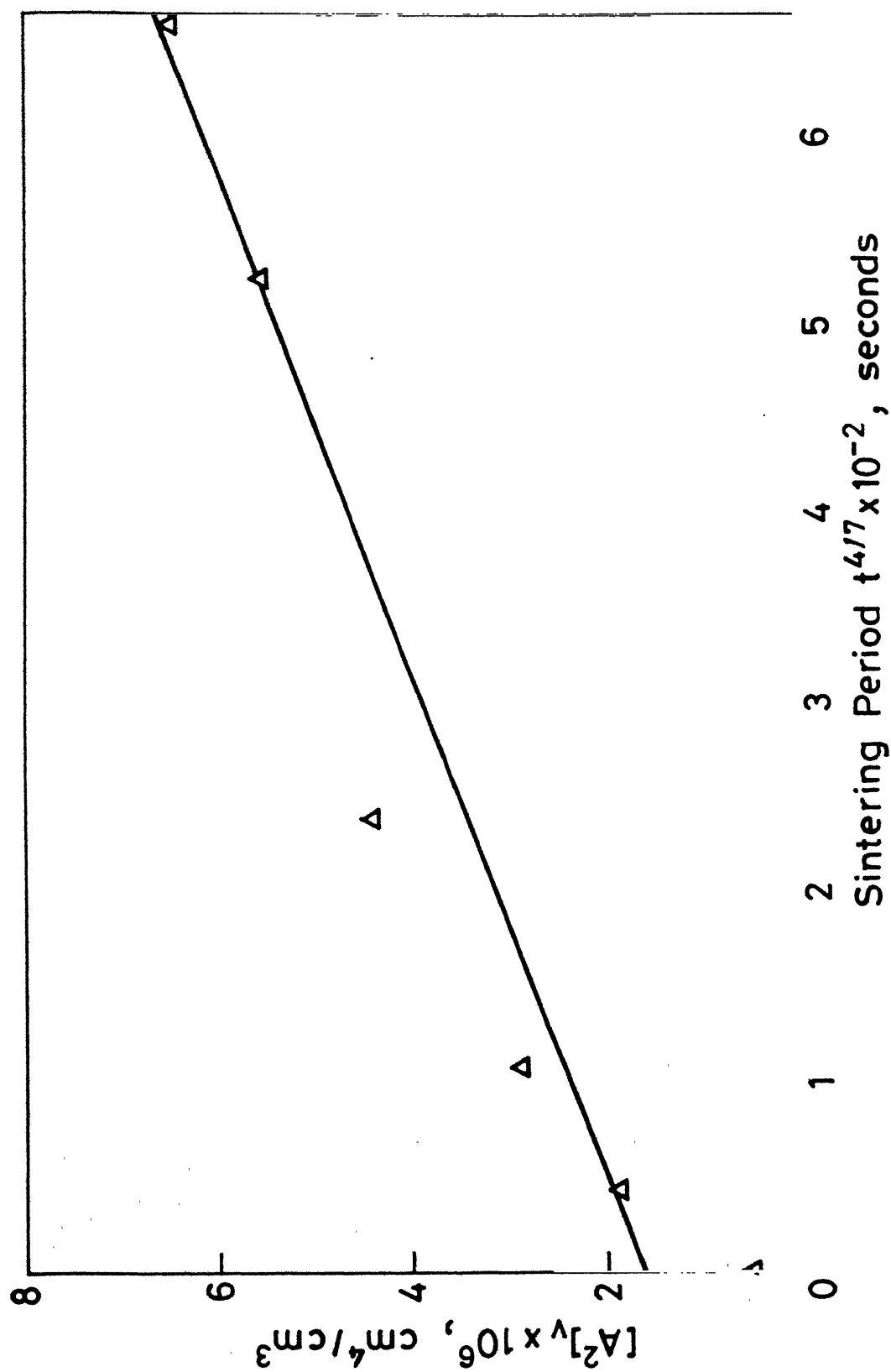


Figure 3.11 A plot of $[A^2]_v$ vs. $t^{4/7}$ during sintering of loose stacked spherical iron powder in hydrogen at 950°C.

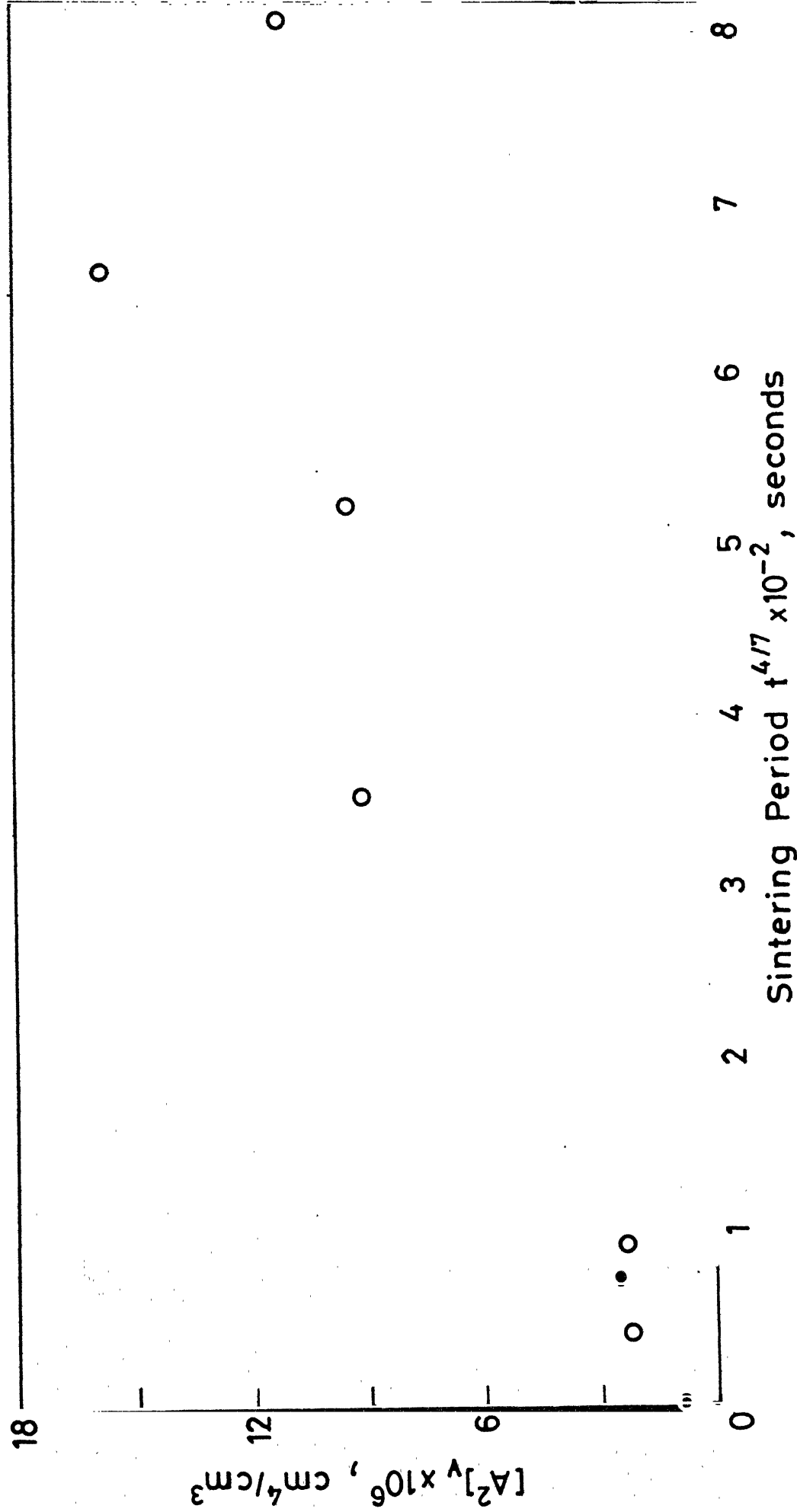


Figure 3.12 A plot of $[A^2]_v$ vs. $t^{4/7}$ during sintering of loose stacked spherical iron powder in hydrogen at 1000°C.

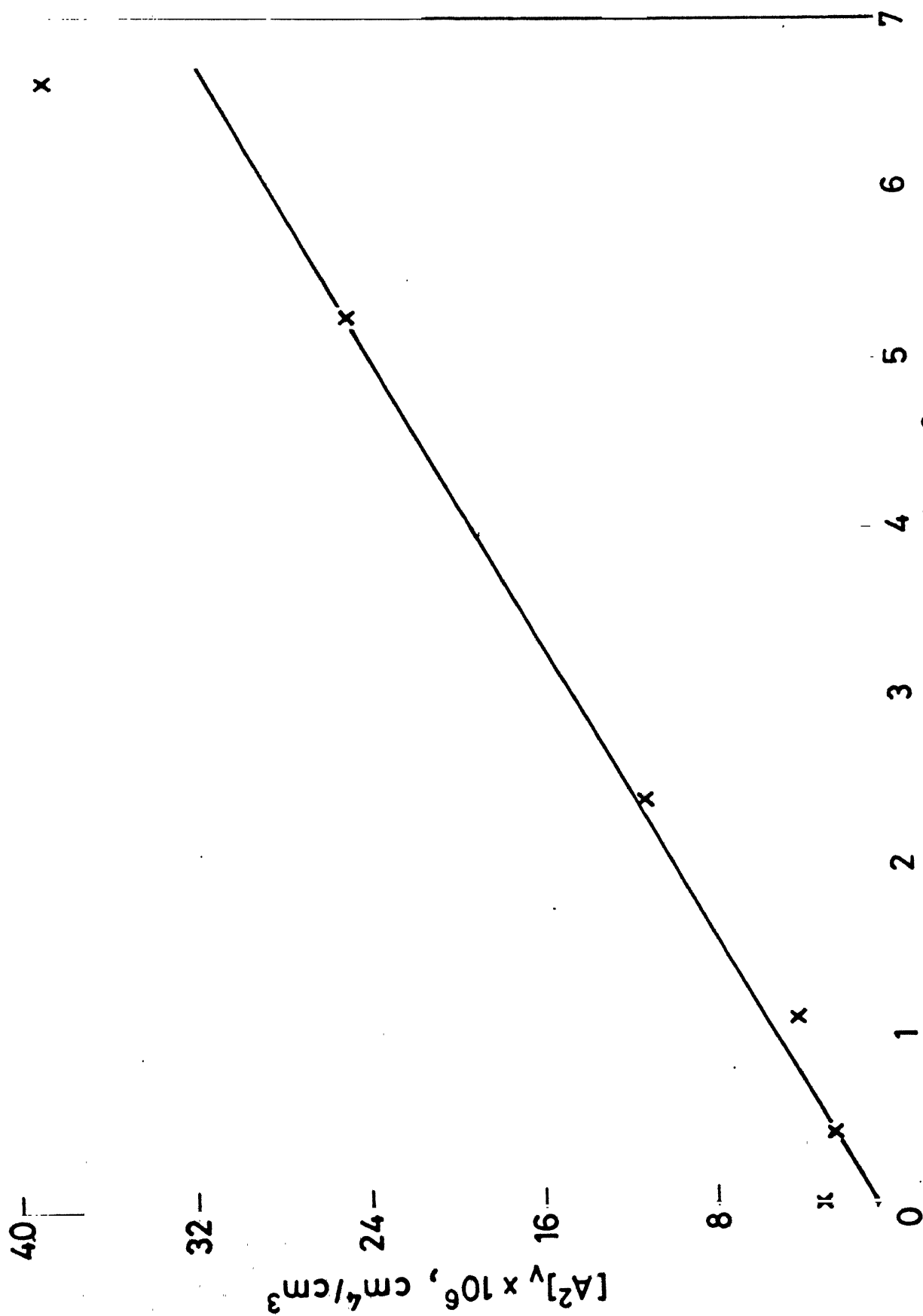


Figure 3.13 A plot of $[A^2]_v$ vs. $t^{4/7}$ during sintering of loose stacked spherical iron powder in hydrogen at 1050°C.

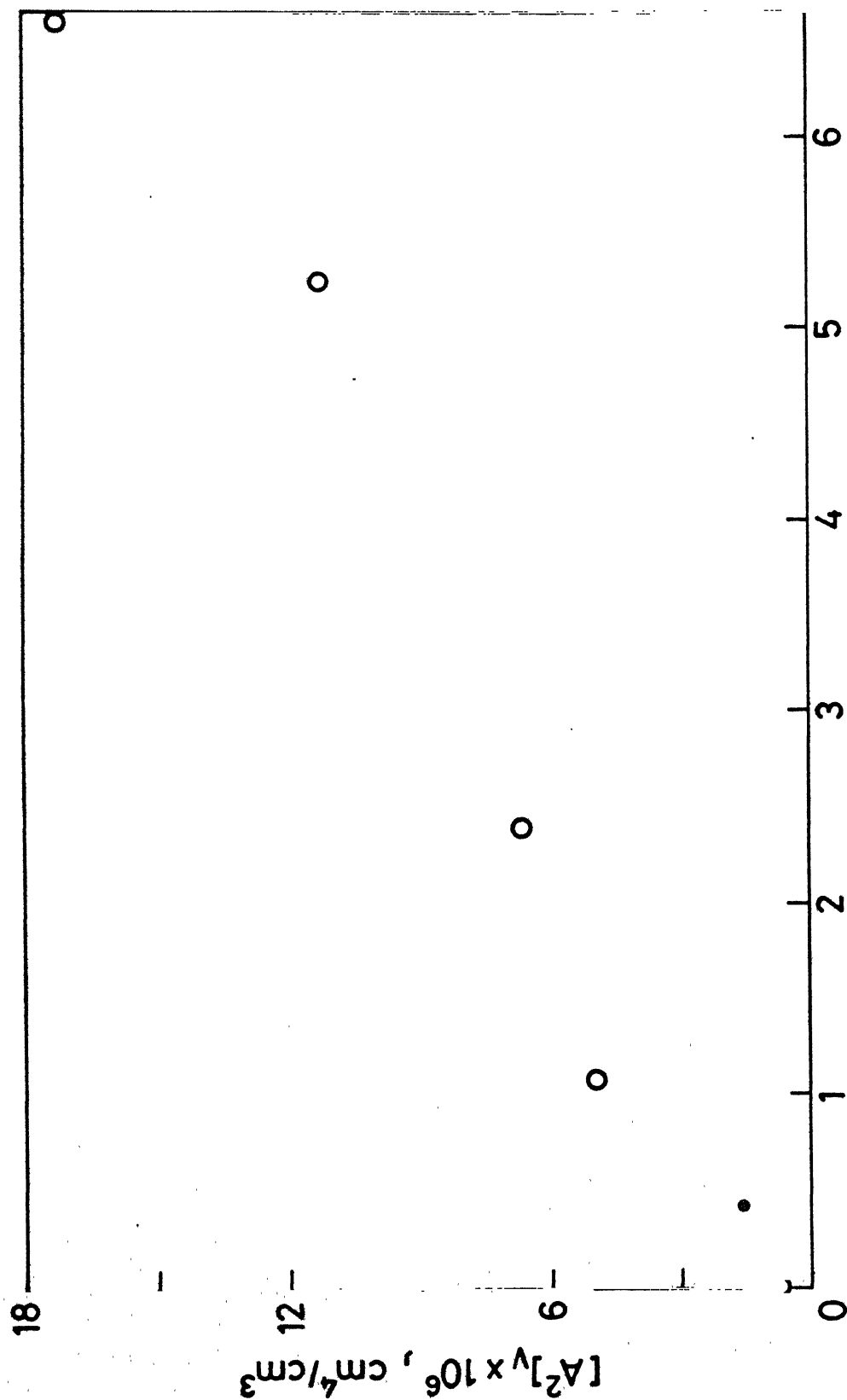


Figure 3.14 A plot of $[A^2]_v$ vs. $t^{4/7}$ during sintering of loose stacked spherical iron powder in argon at 1000°C.

Chapter IV

DISCUSSION

IV.1 VOLUME FRACTION OF POROSITY

From Table 3.1 which provides a comparative picture, it is evident that the sintered porosity values measured by either methods i.e. physical or quantitative metallographic give similar result with a maximum variation of 10%.

As there is no observed shrinkage during the present sintering, it is evident that neck growth is controlled by surface diffusion mechanism. This is clear from Figure 3.1 which shows practically no variation in the porosity level of the sintered compacts upto 34 h of sintering.

IV.2 VARIATION OF OTHER MICROSTRUCTURAL PARAMETERS

If the neck growth is as per the relation given by equation (1.10), then naturally the neck perimeter will also grow accordingly, which can be observed from Figure 3.3 to 3.6, which show plots of L_V against $t^{1/7}$.

The planar area enclosed by neck perimeter varies with $t^{2/7}$ as L_V varies with $t^{1/7}$, which can be concluded from the linearly relation between A_V and $t^{2/7}$ shown in Figures 3.7 to 3.10.

If the neck radius grows with $t^{1/7}$, the $[A^2]_V$, square of planar area enclosed by neck perimeter, should also vary with $t^{4/7}$, which can be deduced from the linearly between $[A^2]_V$ and $t^{4/7}$ (Figures 3.11 to 3.14).

All the above properties i.e. L_V , A_V , $[A^2]_V$ were measured for the powder sintered in hydrogen at 950°C, 1000°C, 1050°C and in argon atmosphere at 1000°C. The slopes of the different plots as given in Figures 3.2 to 3.12 are reported in Table 4.1. The slope of different plots increases with sintering temperature, whereas it is less in H_2 sintered samples as compared to those sintered in argon at 1000°C as it is not expected.

L_V , A_V and $[A^2]_V$ can be represented by

$$L_V = \int_0^{\infty} 2\pi x N_V \cdot dx$$

$$A_V = \int_0^{\infty} \pi x^2 N_V dx$$

$$[A^2]_V = \int_0^{\infty} \pi^2 x^4 N_V dx$$

where x is the radius of neck

N_V is number of neck per unit volume with radius x .

Thus L_V , A_V and $[A^2]_V$ are proportional to the first, second, and the ~~fourth~~ moment of the neck size distribution. Note that in general these three moments should be independent of one another. Thus, L_V , A_V and $[A^2]_V$ are independent microstructural parameters.

According to Kuczynski¹, for surface diffusion controlled growth, the neck radius (x) is related to sintering period (t) as,

$$x = \left(\frac{56 \gamma \delta^4 R^3 D_s}{kT} \right)^{1/7} t^{1/7} \quad (4.1)$$

where γ : surface tension (ergs/cm²)
 δ : interatomic distance (cm)
 R : radius of particle (cm)
 D_s : surface diffusivity (cm²/sec)
 k : Boltzmann constant (ergs/degree)
 T : absolute temperature.

Total perimeter per unit volume (L_V) is given by

$$L_V = 2\pi \times N_V \quad (4.2)$$

where N_V is the number of necks per unit volume with radius x .

Planar area enclosed by neck perimeter (A_V) is given by

$$A_V = \pi x^2 N_V \quad (4.3)$$

Square of planar area enclosed by neck perimeter $[A^2]_V$ is written as,

$$[A^2]_V = \pi^2 x^4 N_V \quad (4.4)$$

Let

$$\alpha = \left[\frac{56 \gamma \delta^4 R^3 D_s}{kT} \right]^{1/7} \quad (4.5)$$

This is the parameter, which gives the idea of kinetics of sintering.

$$x = \alpha \cdot t^{1/7} \quad (4.6)$$

Substituting x obtained by above relation, the equations (4.2-4.4) can be rewritten as,

$$L_V = 2\pi N_V \alpha t^{1/7} \quad (4.7)$$

$$[A^2]_V = \pi^2 N_V \alpha^4 t^{4/7} \quad (4.9)$$

The slope of L_V versus $t^{1/7}$ plot (S_L) becomes

$$S_L = 2\pi N_V \alpha \quad (4.10)$$

Similarly slope of A_V versus $t^{2/7}$ plot

$$S_A = \pi N_V \alpha^2 \quad (4.11)$$

Slope of $[A^2]_V$ versus $t^{4/7}$ plot

$$S_{A^2} = \pi^2 N_V \alpha^4 \quad (4.12)$$

From the equations (4.10) and (4.11) one can get one set of α and N_V given by,

$$\alpha = \frac{2S_A}{S_L} \quad (4.13)$$

$$N_V = \frac{S_L^2}{4\pi S_A} \quad (4.14)$$

and from equations (4.11) and (4.12) another set of α and N_V can be calculated by the relation given by,

$$\alpha = \left[\frac{S_{A^2}}{\pi S_A} \right]^{\frac{1}{2}} \quad (4.15)$$

$$N_V = \frac{(S_A)^2}{S_{A^2}} \quad (4.16)$$

The values of α and N_V calculated from the above two sets of equations, from the experimental results are given in Table 4.2.

As the temperature is increased, the diffusion coefficient also increases which in turn should increase neck growth. It is evident from the slopes (Table 4.1) which increases with

increase in sintering temperature from 950°C to 1050°C.

Neck growth rate is generally greater in reducing atmosphere such as H_2 compared to that in neutral atmosphere (A_V). But in the present study, it is observed from the slopes of plots L_V versus $t^{1/7}$, A_V versus $t^{2/7}$ and $[A^2]_V$ versus $t^{4/7}$, that the neck growth rate is slightly more in argon than that in hydrogen. But α value which is a kinetic parameter is more in H_2 sintered samples than that in Ar sintered samples. However, there is an increase in N_V in Ar sintered samples as compared to H_2 sintered ones. This means that although neck growth rate is more in H_2 atmosphere as is evident from α value, for some reason more number of necks are formed in argon atmosphere, which gave erratic results.

This can be explained by the following reasons:

- 1) In the initial period of sintering, the driving force is very high, so there is more probability for particle rearrangement and new contact formation.
- 2) Particle rearrangement and new contact formation may occur, which is due to deviation from sphericity, anisotropy of surface energy and asymmetric packing of particles. This effect may be very small.

To support the result established by three independent measurements through the plots L_V versus $t^{1/7}$, A_V versus $t^{2/7}$ and $[A^2]_V$ versus $t^{4/7}$ (Figures 3.3-3.14), the slopes of plots L_V versus $t^{1/7}$ are calculated theoretically assuming the Kuczynski's relation given by equation (1.10). S_L could be calculated theoretically as follows.

$$\text{From equation (4.10), } S_L = 2\pi N_V \alpha$$

where $\alpha = \left(\frac{56\gamma \delta^4 R^3 D_s}{kT} \right)^{1/7}$

Acc. No. A.97988

The different material parameters taken from literature are reported in Appendix I. Interatomic distance δ is calculated from lattice parameter 'a'

according to relation $\delta = \frac{a}{\sqrt{2}}$

Radius of particle: R

In the present study $R \simeq 34 \times 10^{-4}$ cms

Number of necks per unit volume (N_V) is taken from the set calculated from S_A and S_{A^2} and it is an independent value with S_L . For convenience, the values of theoretical α , S_L and N_V from S_A and S_{A^2} are reported in Table 4.3. The agreement between the experimental and theoretical values of S_L , as highlighted earlier, is obvious from Table 4.1 and 4.3 and are summarized in Table 4.4.

Analysis has been done for volume diffusion mechanism also. The neck radius grows with fifth root of sintering period, for volume diffusion controlled sintering. Accordingly L_V versus $t^{1/5}$, A_V versus $t^{2/5}$ and $[A^2]_V$ versus $t^{4/5}$ were plotted for all sintering conditions. Some plots behaved linearly, but some showed systematic variation from linearity. For example plots L_V versus $t^{1/5}$, A_V versus $t^{2/5}$, $[A^2]_V$ versus $t^{4/5}$ for the samples sintered in H_2 at $950^\circ C$ shown in Figures 4.1-4.3. Hence volume diffusion controlled mechanism can be ruled out.

From all the independent parameters discussed namely L_V , A_V and A^2_V , it can be concluded that the neck growth equation given by equation (4.10) is also applicable in the real powder mass of narrow size range.

Table 4.1

Variation of Slopes in Plots Obtained after measurements with respect to Sintering Temperature, Atmosphere

Sintering temperature atmosphere	Slope of L_V vs. $t^{1/7}$ plot (S_L) $\times 10^{-3}$, $\text{cm}^{-2} \cdot \text{sec}^{-1/7}$	Slope of A_V vs. $t^{2/7}$ plot (S_A), $\text{cm}^{-1} \cdot \text{sec}^{-2/7}$	Slope of $[A^2]_V$ vs. $t^{4/7}$ plot (S_{A^2}) $\times 10^8$, $\text{cm} \cdot \text{sec}^{-4/7}$
950°C, H_2	2.95	0.16	0.76
1000°C, H_2	4.58	0.32	1.91
1050°C, H_2	7.74	0.65	4.57
1000°C, Ar	5.64	0.38	2.27

Table 4.2

Variation of α and N_V from two Separate Sets of Slopes (Eq. 4.13-4.16) after Quantitative Metallographic Measurements

Sintering temperature, atmosphere	From S_L and S_A		From S_A and S_{A^2}	
	α $\times 10^4$, $\text{cm} \cdot \text{sec}^{-1/7}$	N_V $\times 10^{-6}$, cm^{-3}	α $\times 10^4$, $\text{cm} \cdot \text{sec}^{-1/7}$	N_V $\times 10^{-6}$, cm^{-3}
950°C, H_2	1.0799	4.3500	1.2352	3.3257
1000°C, H_2	1.4144	5.1572	1.8788	5.4909
1050°C, H_2	1.6742	7.3596	1.4990	9.1811
1000°C, Ar	1.3519	6.6410	1.3756	6.4142

Table 4.3

Variation of Theoretically Calculated Values

Sintering temperature, atmosphere	N_V from S_A and $S_A^2 \times 10^{-6}, \text{cm}^{-3}$	α (by the relation (4.5)) $\times 10^4, \text{cm} \cdot \text{sec}^{-1/7}$	$S_L = 2\pi N_V \alpha \times 10^{-3}, \text{cm}^{-2} \cdot \text{sec}^{-1/7}$
950°C, H_2	3.33	2.78	5.81
1000°C, H_2	5.49	3.18	12.17
1050°C, H_2	9.18	3.59	20.71
1000°C, Ar	6.41	2.90	11.69

Table 4.4

Summary of S_L Values after Experimental and Theoretical Considerations

Sintering temperature, atmosphere	Experimental $\times 10^{-3}, \text{cm}^{-2} \cdot \text{sec}^{-1/7}$	Theoretical $\times 10^{-3}, \text{cm}^{-2} \cdot \text{sec}^{-1/7}$
950°C, H_2	2.95	5.81
1000°C, H_2	4.58	12.17
1050°C, H_2	7.74	20.71
1000°C, Ar	5.64	11.69

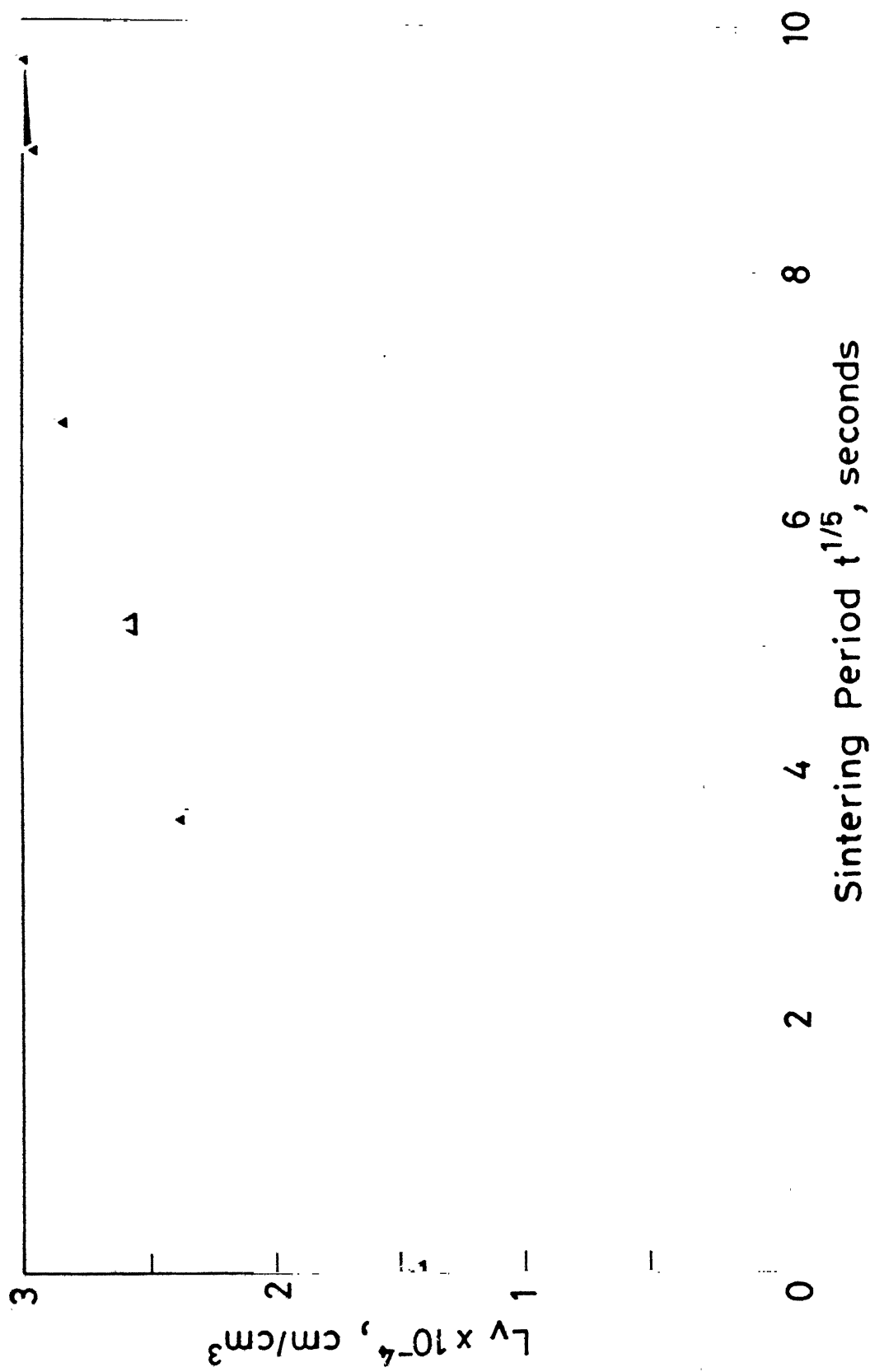


Figure 4.1 A plot of L_v vs. $t^{1/5}$ during sintering of loose stacked spherical iron powder in hydrogen at 950°C.

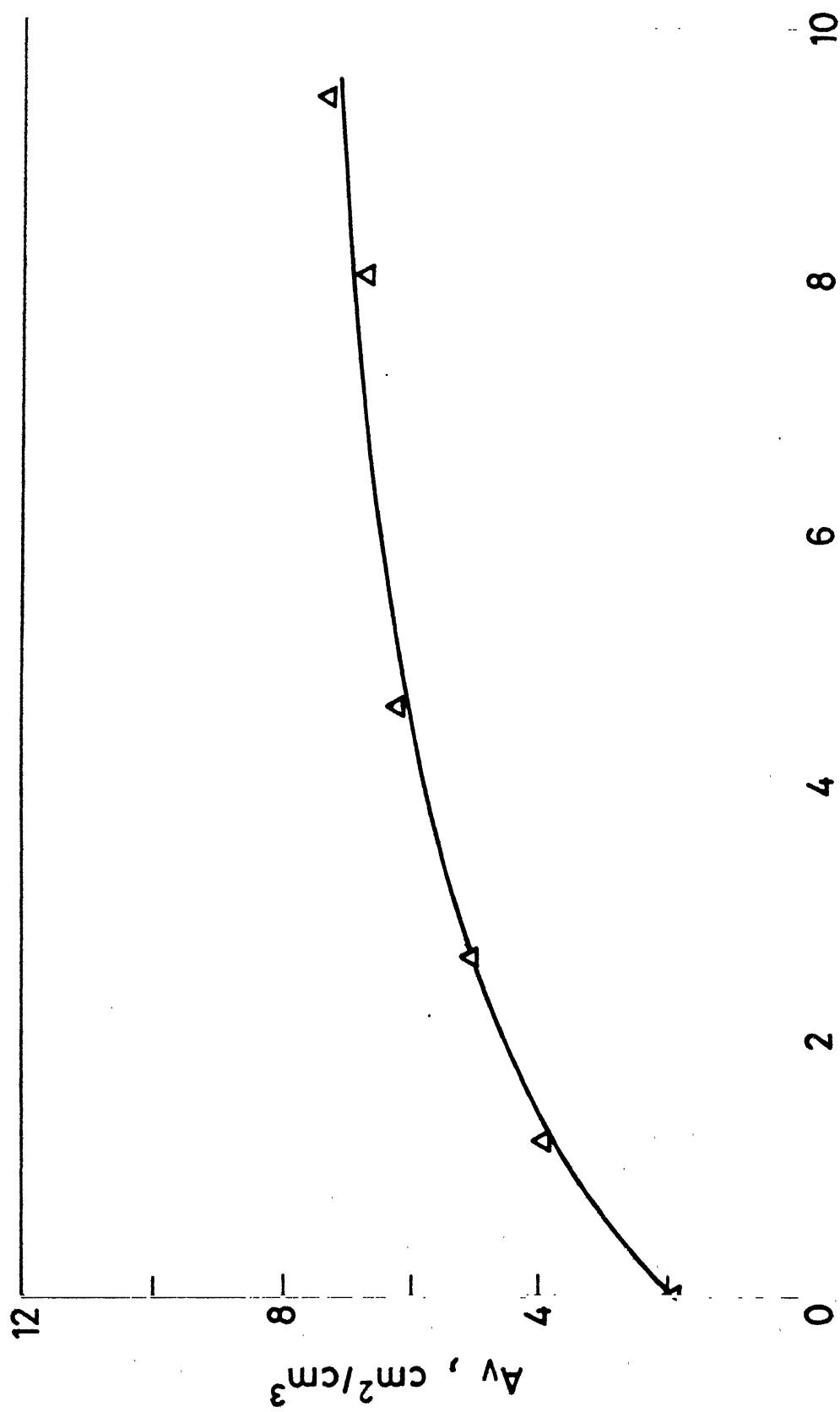


Figure 4.2 A plot of A_v vs. $t^{2/5}$ during sintering of loose stacked spherical iron powder in hydrogen at 950°C .

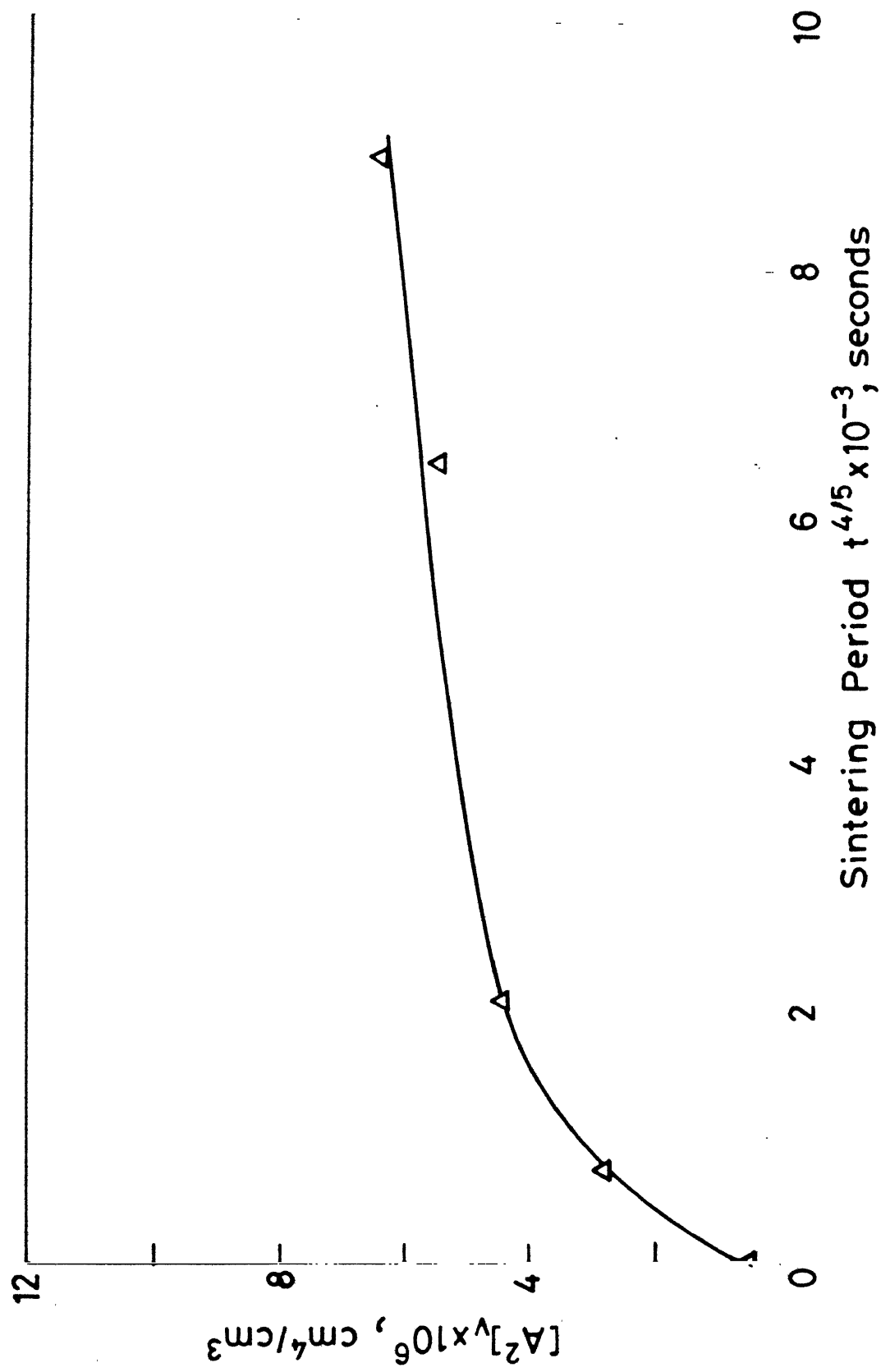


Figure 4.3 A plot of $[A^2]_v$ vs. $t^{4/5}$ during sintering of loose stacked spherical iron powder in hydrogen at 950°C .

Chapter V

CONCLUSIONS

- (1) Since the volume fraction of pores does not vary with sintering time upto 34 h, it may be concluded that the sintering kinetics is controlled by surface diffusion.
- (2) The microstructural evolution of the interparticle necks can be quantified in terms of microstructural parameters L_V , A_V , $[A^2]_V$ which can be estimated unambiguously from the measurements performed on the plane of polish without making any simplifying assumptions regarding particle shape or size.
- (3) The behaviour of experimental data shows that L_V , A_V and $[A^2]_V$ vary linearly with $t^{1/7}$, $t^{2/7}$, $t^{4/7}$ respectively during isothermal sintering in the temperature range investigated in the present work. This strongly supports surface diffusion as rate controlling mechanism. This is particularly so because it has been conclusively shown that volume diffusion controlled sintering is not operative.
- (4) The experimental and theoretical values of the kinetic parameter α for surface diffusion controlled mechanism agree within a factor of two. This demonstrates qualitative agreement of the experimental with the theoretical predictions. The discrepancy of factor of two perhaps arises due to
 - (a) the measurement errors

(b) uncertainties in the values of parameters D_s , γ etc. which determine α

(c) the analysis is based on monosized powder mass.

However the powder does consist of narrow size range having particle sizes in the range $62 \mu - 74 \mu$. To the best knowledge of author this is the first demonstration of quantitative agreement between all aspects of the theory of surface diffusion controlled sintering and the experimental behaviour in the powder mass of narrow size range.

(5) The number of interparticle contacts N_v does not vary significantly with sintering time, this indicates that the contact formation basically occurs in very initial stages of the process.

(6) From the results it is apparent that the neck growth rate is less in argon sintered samples compared to that in hydrogen sintered samples which is evident from kinetic parameter α .

REFERENCES

1. G.C. Kuczynski, Trans. AIME, 185 (1949) 169.
2. H.E. Exner, Reviews on Powder Metallurgy and Physical Ceramics, 1 (1979).
3. G.C. Kuczynski, J. Appl. Physics, 20 (1949) 1160.
4. G.C. Kuczynski, J. Appl. Physics, 21 (1970) 632.
5. A.L. Pranatis and L. Seigle, "Powder Metallurgy", edited by W. Leszynski, Interscience Publishers (1961) p. 53.
6. W.P. Kingerry and M. Berg, J. Appl. Physics, 26 (1955) 1205.
7. D.L. Johnson, Physics of Sintering, 1 (1969) No. 1, B1.
8. D.L. Johnson, J. Appl. Physics, 40 (1969) 192.
9. M.F. Ashby, Acta Meta., 22 (1974) 275.
10. N. Cabrera, Trans. AIME, 188 (1950) 667.
11. P. Schwed, Trans. AIME, 191 (1951) 245.
12. J.G.R. Rockland, Acta Meta., 14 (1966) 1273.
13. D. Uskokovic and H.E. Exner, Science of Sintering, 9 (1977) 265.
14. G.C. Kuczynski, Science of Sintering, 9 (1977) 243.
15. R.T. DeHoff and F.N. Rhines, Quantitative Microscopy, McGraw Hill, N.Y., 1968.
16. E.E. Underwood, Quantitative Stereology, Addison-Wesley, Reading, Mass., 1970.
17. A.M. Gokhale, Communicated to Metallography.
18. M.C. Inman and H.R. Tipler, Met. Rev., 8 (1963) 105.
19. W.B. Pearson, Handbook of Lattice Spacings and Structures of Metals, Pergamon Press.
20. G. Neumann and G.M. Neumann, Surface Self-Diffusion of Metals, Diffusion Monograph Series 1, 1972.

Appendix IMATERIAL PARAMETERS FROM LITERATURE USED
IN THEORETICAL CALCULATIONS

The surface free energy for iron $\gamma \simeq 2000 \text{ ergs/cm}^2$ Ref.: 18

Boltzmann constant $k = 1.38 \times 10^{-16} \text{ ergs/degree}$

Lattice parameters and surface diffusivities:

Temperature, atmosphere	Lattice parameter (a) ¹⁹ X10 ⁻⁸ , cms	Surface self-diffusivity (D _s) ²⁰ X10 ⁵ , cm ² /sec
950°C, H ₂	3.6496	1.1158
1000°C, H ₂	3.6537	2.9237
1050°C, H ₂	3.6578	7.1232
1000°C, Ar	3.6537	1.5452

This book is to be returned on the
date last stamped.

[illegible]

ME.-1987 - M - BAS - STE

Thesis
671.373
B29-S

A97988